*remote sensing*

MDPI

*Article*

# The Potential of Multibeam Sonars as 3D Turbidity and SPM Monitoring Tool in the North Sea

**Nore Praet [1,*], Tim Collart [2], Anouk Ollevier [1], Marc Roche [3], Koen Degrendele [3], Maarten De Rijcke [1], Peter Urban [4,5] and Thomas Vandorpe [1]**

1 Flanders Marine Institute (VLIZ), InnovOcean Campus, Jacobsenstraat 1, 8400 Ostend, Belgium; anouk.ollevier@vliz.be (A.O.); maarten.de.rijcke@vliz.be (M.D.R.); thomas.vandorpe@vliz.be (T.V.)
2 Seascape Belgium, InnovOcean Campus, Jacobsenstraat 1, 8400 Ostend, Belgium; tim.collart@seascapebelgium.be
3 Federal Public Service Economy, Continental Shelf Service, Koning Albert II Laan 16, 1000 Brussels, Belgium; marc.roche@economie.fgov.be (M.R.); koen.degrendele@economie.fgov.be (K.D.)
4 Department of Geology, Ghent University, Krijgslaan 281 (S8 WE13), 9000 Ghent, Belgium; peter.urban@ugent.be
5 Department of Data Analysis and Mathematical Modelling, Ghent University, Coupure links 653, 9000 Ghent, Belgium
* Correspondence: nore.praet@vliz.be

**Abstract:** Monitoring turbidity is essential for sustainable coastal management because an increase in turbidity leading to diminishing water clarity has a detrimental ecological impact. Turbidity in coastal waters is strongly dependent on the concentration and physical properties of particles in the water column. In the Belgian part of the North Sea, turbidity and suspended particulate matter (SPM) concentrations have been monitored for decades by satellite remote sensing, but this technique only focuses on the surface layer of the water column. Within the water column, turbidity and SPM concentrations are measured in stations or transects with a suite of optical and acoustic sensors. However, the dynamic nature of SPM variability in coastal areas and the recent construction of offshore windmill parks and dredging and dumping activities justifies the need to monitor natural and human-induced SPM variability in 3D instead. A possible solution lies in modern multibeam echosounders (MBES), which, in addition to seafloor bathymetry data, are also able to deliver acoustic backscatter data from the water column. This study investigates the potential of MBES as a 3D turbidity and SPM monitoring tool. For this purpose, a novel empirical approach is developed, in which 3D MBES water column and in-situ optical sensor datasets were collected during ship transects to yield an empirical relation using linear regression modeling. This relationship was then used to predict SPM volume concentrations from the 3D acoustic measurements, which were further converted to SPM mass concentrations using calculated densities. Our results show that these converted mean mass concentrations at the Kwinte and Westdiep swale areas are within the limits of the reported yearly averages. Moreover, they are in the same order of magnitude as the measured mass concentrations from Niskin water samples during each campaign. While there is still need for further improvement of acquisition and processing workflows, this study presents a promising approach for converting MBES water column data to turbidity and SPM measurements. This opens possibilities for improving future monitoring tools, both in scientific and industrial sectors.

**Keywords:** turbidity; suspended particulate matter; multibeam water column; LISST-200X



**Citation:** Praet, N.; Collart, T.; Ollevier, A.; Roche, M.; Degrendele, K.; De Rijcke, M.; Urban, P.; Vandorpe, T. The Potential of Multibeam Sonars as 3D Turbidity and SPM Monitoring Tool in the North Sea. *Remote Sens.* **2023**, *15*, 4918. https://doi.org/10.3390/rs15204918

Academic Editors: Jiayi Pan and Zhe-Wen Zheng

Received: 23 August 2023
Revised: 2 October 2023
Accepted: 8 October 2023
Published: 11 October 2023



## 1. Introduction

Turbidity expresses the degree to which water loses its transparency due to the scattering and absorption of light by suspended particles [1,2]. It is an important indicator of water quality that is fundamental to the research, management, and protection of coastal

ecosystems. Monitoring turbid areas is vital as excessive turbidity is known to have a detrimental ecological impact [3,4]. Changes in turbidity will directly affect primary production and modulate predator-prey relationships, causing knock-on effects that can be measured throughout the entire marine food web [3,5].

Another major component of coastal monitoring is suspended particulate matter (SPM), which is highly linked to turbidity. It comprises a wide variety of sub-2-mm sized particles that are either biogenic (living phyto- and zooplankton and dead organic matter) or sedimentological (physico-chemical and biogenic minerals, mainly resuspended surface sediments) [6–8]. Often, the organic biomass and sediments interact with each other by forming larger aggregates (flocs), changing the fate and transport of SPM [9–11].

Optical turbidity and SPM concentrations are traditionally determined through the analysis of water bottle samples. However, these techniques are time consuming, and the resulting measurements are non-continuous. Therefore, more efficient techniques have emerged using a wide range of optical (e.g., Optical Backscatter Sensor (OBS) and Laser In-situ Scattering and Transmissometer (LISST)) and acoustic (e.g., Acoustic Doppler Current Profiler (ADCP)) sensors [12–16] that collect continuous turbidity and SPM datasets in-situ. Gravimetric and optical turbidity measurements of discrete water samples in the lab are then used for ground-truthing [17–23].

In the Belgian part of the North Sea (BPNS), SPM concentrations vary seasonally with higher concentrations in winter and lower concentrations in summer. This seasonal SPM signal is predominantly controlled by the biological cycle (phytoplankton blooms in spring and early summer) [10]. Furthermore, human activities such as the construction of offshore windmill parks [24] and dredging and dumping activities [25,26] are known to have far-field effects and may significantly increase SPM variability. Improving our understanding of both natural and human-induced SPM variability is therefore essential for sustainable coastal management. Large spatial datasets of optical turbidity and SPM patterns in the North Sea have been derived for years by remote sensing of ocean color [11,27–29]. However, these datasets are restricted to the surface layer of the water column, whereby the penetration depth depends on the wavelength of the signal and the amount of sediment in suspension [29]. Within the water column, optical (LISST, OBS) and acoustic (ADCP) sensors are used to measure SPM in the BPNS in both stations [9,24,30,31] and transects [32,33]. However, coastal and near-shore areas, such as the BPNS, are dynamic environments where SPM patterns can exhibit fluctuations across all four dimensions of spacetime [9,10]. Hence, there is a clear urgency to monitor these SPM changes in 3D. A possible solution lies in multibeam echosounder (MBES) technology, which is based on the emission of sound pulses in a swath.

In the past decades, acoustic backscatter systems (ABS) [34–36] and ADCP instruments [37,38] have demonstrated the quantitative use of acoustics for suspended sediment studies using acoustic inversion approaches that convert high-frequency acoustic data to SPM concentrations in sandy [34,39,40] and cohesive regimes [35,41,42]. In situ water samples are frequently used to calibrate and quantify ADCP measurements in stationary profiles [20,43–45] or in transects [21,22,46–49] through model parameter calibration (regression between sensor output signal and real SPMC). While the potential of these ABS and ADCP instruments for SPM monitoring is well-studied, only a handful of studies have used MBES sonars to quantify suspended sediments in the water column [50–54]. The scarcity of MBES-focused SPM studies is mainly due to the complex nature of particle scattering and the difficulty of dealing with large data volumes. MBES systems are generally used to retrieve depth and characteristics of the seabed [55]. However, when sound pulses travel through the water, they also interact with targets (suspended particles, fish, gas bubbles, etc.) within the water column. Thanks to advances in storage capacity and processing power, MBES can nowadays also deliver a 3D dataset of acoustic measurements in the water column [56]. This new MBES-based approach to visualize the water column has been embraced by a myriad of applications, including fisheries [57], gas seep-

age [58], shipwreck research [59], sediment plumes induced by dredging activity [60], and turbidity currents [48].

This study presents a novel methodology to convert MBES water column data into a 3D visualization of turbidity and SPM measurements. In contrast to most studies that deploy the MBES from stationary (moored) vessels, we quantify SPM using MBES from a moving vessel. For this purpose, we chose to follow an empirical approach for the characterization of suspended sediments by collecting simultaneous optical and acoustic measurements while sailing in a natural environment, i.e., the BPNS [8–10,31], where SPM concentration and composition vary spatially and temporally (tidal cycle/seasons). Finally, this paper also shares valuable lessons that were learned during this study. This will contribute to open up new prospects for using multibeam sonars as a future monitoring tool for SPM.

## 2. Study Area

Five campaigns were conducted with the RV Simon Stevin (RVSS) in the Kwinte and Westdiep swale areas during autumn/winter (October 2020, February 2021) and spring/summer (March 2021, May 2021, July 2021) (Figure 1). During each campaign, large datasets of 3D MBES water column and in situ optical sensor data were collected simultaneously (Appendix A).

In each campaign, measurements were taken close to the Kwinte acoustic reference area [61,62] (Figure 1, Appendix A), situated in the western part of the Belgian part of the North Sea (BPNS). This area was selected as it is situated at the edge of the winter turbidity maximum zone, resulting in pronounced seasonal changes in surface SPM (and linked chlorophyll-a) concentrations [10]. Furthermore, the Kwinte acoustic reference area is protected from bottom-disturbing activities. The Kwinte area is also located close to shore (about 16 km, ensuring limited transit times) and exhibits a uniform (sandy to gravelly) geology and bathymetry (25 m Lowest Astronomical Tide; LAT) [61,63]. These water depths allow safe undulating movements of the in situ sensors in the water column. During the July 2021 campaign, the Westdiep area (Figure 1, Appendix A), located 5 km offshore in water depths of about 15 m LAT, was surveyed due to adverse conditions in the Kwinte area.

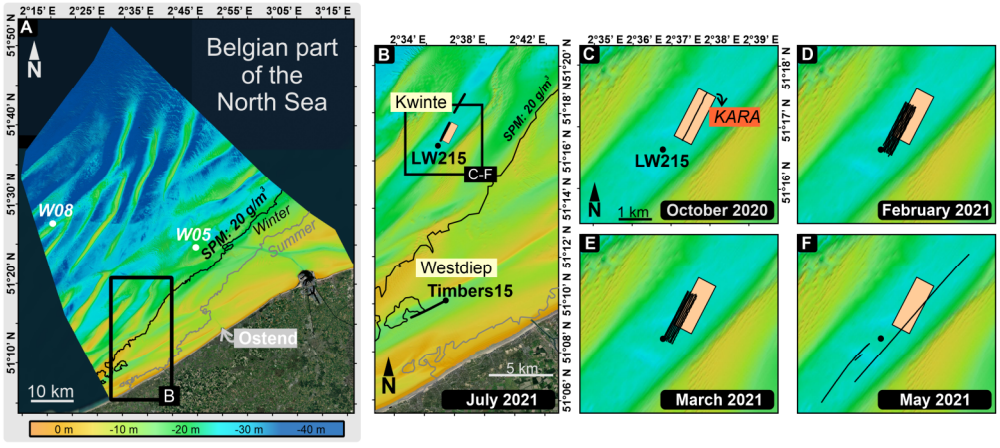


**Figure 1.** (**A**) The Belgian part of the North Sea: 20 m bathymetric grid from Maritime and coastal services-Flemish hydrography [64], with indication of stations W05 (51°25.000′N, 2°48.500′E) and W08 (51°27.610′N, 2°20.910′E) and the 20 g/m$^3$ SPM concentration contours in winter (black) and summer (grey) [10]. (**B**) Detail of the Kwinte and Westdiep study areas with indications of the July 2021 survey lines. (**C**–**F**) Detail of the Kwinte study area with the survey lines for the October 2020 (**C**), February 2021 (**D**), March 2021 (**E**) and May 2021 (**F**) campaigns. The location of the Kwinte acoustic reference area (KARA) and water sampling stations LW215 and Timbers 15 are indicated.

## 3. Materials and Methods

### *3.1. Data Acquisition*

#### 3.1.1. MBES–System and Settings

Large MBES water column datasets were collected using an EM2040 dual Rx (MKII) system (Kongsberg, Norway), hull-mounted on the RVSS (Figure 2). This shallow-water MBES consists of one transmitter Tx (0.4°) and two receiver Rx (0.7°) transducers in Mills Cross Configuration [65]. The system can be operated with a frequency range of 200–400 kHz, and maximum 200° swath coverage, consisting of 800 beams with 0.4° × 0.7° beam width (400 kHz).

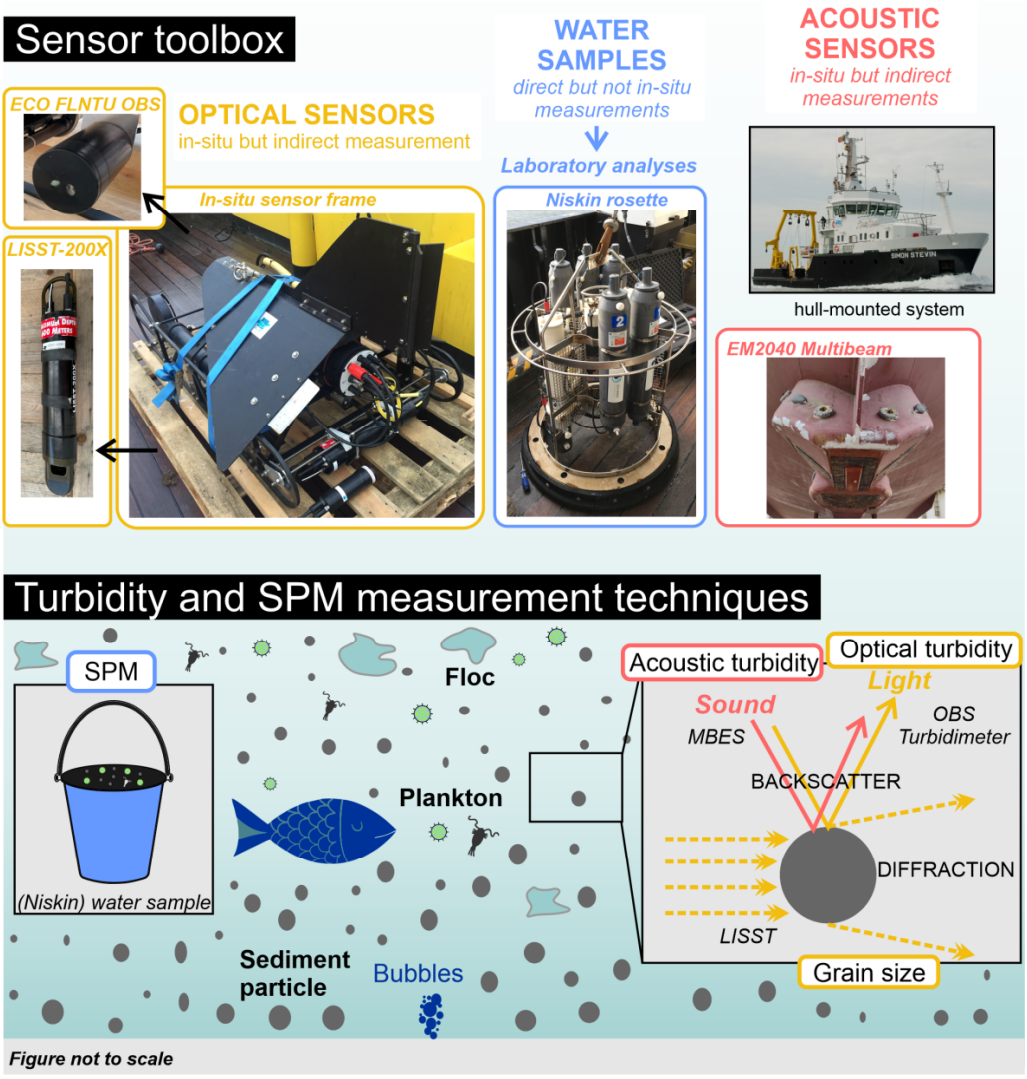


**Figure 2.** (**Top**)—the sensor toolbox used within this study comprises optical (LISST-200X, Eco FLNTU OBS) and acoustic (EM2040 MBES hull-mounted on RV Simon Stevin) sensors, as well as (Niskin) water samples. (**Bottom**)—overview of turbidity and SPM measurement techniques based on different principles: acoustic backscatter (MBES), optical backscatter (OBS), laser diffraction (LISST) and filtration of discrete water samples (Niskin).

The same set of configuration parameters is consistently applied to the MBES throughout all surveys in order to ensure comparability of the different acoustic datasets. The MBES was used in single sector mode to avoid the use of different frequencies for the different emission sectors. The highest possible frequency (400 kHz), the long pulse length (54 µs), and no filters were chosen to maximize the signal-to-noise-ratio. The swath widths of both receivers were limited to avoid overlap (RX Port: −65–0°; RX Starboard: 0–65°) and equian-

gular beam spacing was chosen to spread the receive beams equally over the entire water column. The maximum ping rate was limited to 10 Hz to keep the datasets manageable. For more details on the setup, see Supplementary Document S1. For georeferencing of the beam samples, we used pre-computed sound velocity profiles that were regularly matched against the surface sound speed measured by the vessel. This is standard procedure for bathymetric surveys in the area and works well because tidal mixing causes the water column to be homogeneous without significant stratification.

#### 3.1.2. In Situ Sensor Toolbox: Settings and Deployment

In situ optical (turbidity) measurements were produced with a LISST-200X (Sequoia Scientific Inc., Bellevue, WA, USA) and an Eco FLNTU OBS (Sea-Bird Scientific, Bellevue, WA, USA), mounted on a towed, stable frame (Seascan Inc., Falmouth, MA, USA) (Figure 2). The LISST-200X measures particle size distributions in 36 grain-size classes (1–500 µm) and the total volume concentration (TVC; in µL/L) using the principle of laser diffraction (forward scattering) [66]. The LISST was deployed horizontally (Figure 2) and oriented in such a way that the horizontal water current was minimally obstructed in order to avoid the creation of bubbles and vortices in the measurement chamber [67]. The sampling rate was set to 1 s, averaging over 30 measurements, to ensure adequate coverage of the water column over this time period (Supplementary Document S2). The Eco FLNTU OBS measures optical turbidity (in NTU) at 700 nm wavelength using the principle of optical backscattered light at 140 degrees. The raw OBS output can be expressed in optical turbidity (NTU) by applying an instrument-specific scale factor.. Measurements were made every 40 ms. The resulting raw in situ sensor datasets can be consulted on the Marine Data Archive (MDA) [68].

#### 3.1.3. Sensor Sensitivity

All of the acoustic and optical sensors measure turbidity and suspended particles in the water column but use different measurement principles (Figure 2). MBES is based on the principle of acoustic backscatter, while the optical sensors use the principle of laser diffraction (LISST) and optical backscattering (OBS). Consequently, different sensors inherently have different particle types and size sensitivities, which leads to sensor-dependent particle-detection.

The responsiveness of optical and acoustic backscatter instruments is linked to the different particle properties (size, shape, and composition) (Haalboom et al. [17]; and the references therein). Optical backscatter systems are more sensitive to cohesive low-density, irregularly-shaped mud particles and flocs, as their area-to-volume ratio results in a larger projected area and thus a higher backscatter signal [17,69–72].

In contrast, the interaction between an acoustic pulse and particles is optimal for coarse (>63 µm), high-density, spherical sand grains [73]. For acoustic backscatter systems, the backscatter response to different particle sizes also relies on the operating frequency (f), with lower frequencies being less sensitive to smaller particles than higher frequencies [74]. Acoustic sensors have peak sensitivity for particles with a diameter $d = 2/k$, which is based on the wave number $k = 2\pi f/c$ [17,73,75]. For particles smaller than this peak diameter, the sensitivity (at a given particle concentration) is expected to decrease with a fourth power law [76]. Hence, the MBES 400 kHz frequency used in this study should provide optimal acoustic scattering for grain sizes around 1200 µm, while the sensitivity for grain sizes with 60 µm is expected to be reduced by ~52 dB.

The LISST-200X measures particles with grain sizes between 1–500 µm. When particles fall outside this measurement range, a rising tail is produced at the lower and upper end of the particle size spectrum [10,77,78]. In general, no issues with out-of-range particles are expected because the large LISST-200X measurement range overlaps with the size ranges of particles in the North Sea [10]. Furthermore, the particle's refractive index and shape can be responsible for inventing small particles that attribute to the rising tail at the fine

end of the LISST size spectrum [77,79,80]. We minimized these rising tail artefacts by using a kernel matrix derived from random-shaped particles [77].

#### 3.1.4. Sampling Strategy

To collect data from all sensors simultaneously, we implemented an innovative sampling strategy (Figure 3). MBES data was recorded during ship transects. Simultaneously to this recording, we used the in situ sensor frame to perform undulating "yoyo" movements between 5 and 20 m water depth. The vertical descent and ascent rate of the in situ sensor frame was kept as low as possible, being around 20 cm/s. Artefacts in the MBES data were minimized by sailing in a straight line at low constant speed (~3 knots) and by refraining from using other echosounders or bow propellers.

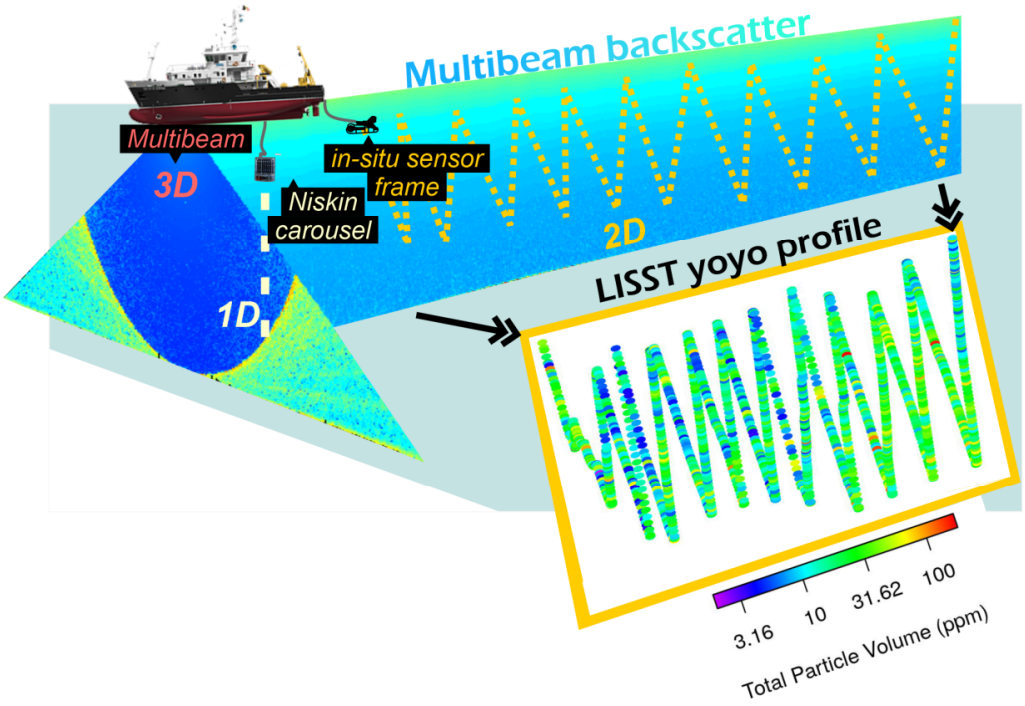


**Figure 3.** Overview of the sampling strategy: continuous recording of MBES water column data, yoyo-movement of the in-situ sensor frame (with attached turbidity sensors), and Niskin bottle deployments.

The continuous acoustic and optical sensor measurements were validated by the collection and analysis of discrete Niskin water samples in each campaign except for the October 2020 campaign. The water samples were collected from various depths in stations located in the Kwinte or Westdiep areas, respectively LW215 (51°16.648′N; 2°36.797′E) and Timbers 15 (51°10.160′N; 2°37.375′E) (Figure 1, Appendix A). These stations were visited minutes to hours before the simultaneous acoustic and optical measurements (survey lines indicated in Figure 1). Filtration and gravimetric analyses of the Niskin water samples yielded suspended particle concentrations in mg/L (with a precision of 0.1 mg/L). These laboratory analyses were performed by the Flanders Environment Agency (VMM), following their standard protocol. The dataset can be consulted on MDA [68].

### *3.2. Data Processing*

#### 3.2.1. MBES Data

Processing of large quantities of MBES water column data was conducted in a specialized MATLAB-based software called SonarScope (Version R2021a) (Ifremer, Plouzané, France) [81]. Since the study of MBES water column data is an emerging discipline, we, in consultation with the developer, created a tailor-made data processing pipeline to

visualize and export MBES water column data as 3D point clouds (Figure 4). The detailed step-by-step procedure (for .all file format) is provided in Supplementary Materials (Supplementary Document S3).

The data format of Kongsberg delivers the WC data in {Sample,Beam} geometry, i.e., for every beam, a series of echoes (in dB) are displayed over time. However, for further interpretation {Depth, AcrossDistance}, geometry is recommended (Figure 4). Polar echograms were created by masking all soundings below the bottom detection, georeferencing the beam samples (including raytracing), applying the tide correction, and finally by converting the raw beam amplitudes into (uncalibrated) volume backscattering strength values, $S_v$ (in dB). For the last step, SonarScope applied the same conversion approach as described in equation 9 in Urban et al. [58].

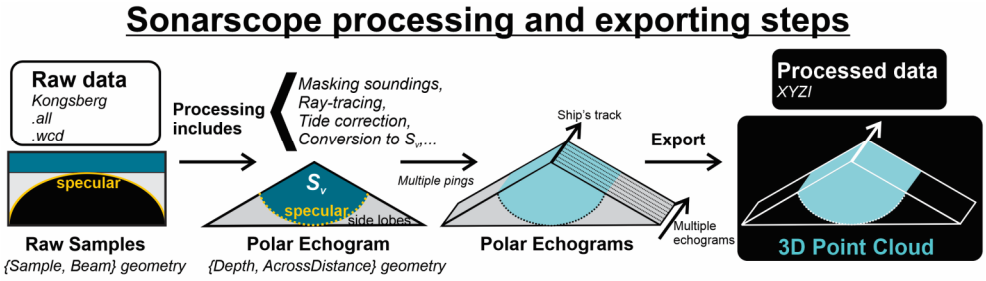


**Figure 4.** Processing steps of water column MBES data in SonarScope. The polar echograms were modified after Urban et al. [58].

Ideally, the MBES system should be calibrated towards absolute decibel values to ensure comparability of acoustic datasets between different surveys (absolute calibration [82]). Furthermore, the beams of the system should be intercalibrated to measure $S_v$ uniformly over the entire fan (relative calibration; [82]). Unfortunately, this MBES calibration is difficult and time consuming, especially for hull-mounted multibeam systems [53,54,83,84]. Therefore, as with the vast majority of MBES, the RV Simon Stevin MBES water column data are not calibrated. Consequently, absolute $S_v$ values cannot be calculated. Instead, qualitative $S_v$ were calculated [58], which differ from calibrated $S_v$ by a constant calibration factor. Since the same MBES was used and the settings were kept fixed for each campaign, we do not expect significant differences of the absolute calibration factor for the different campaigns. However, due to the missing relative calibration, it is possible that differences in the calibration between beams occur. This can influence the comparability of the measurements at different beam angles.

Every polar echogram is affected by prominent noise that is inherent to the beam pattern of the sonar system [58,85,86]. Transmit and receive beam patterns are not perfectly directional, so although the strongest sensitivity of each beam occurs in the main direction (main lobe), the beams will also be sensitive in other directions (side lobes). Backscatter signals caused by echoes coming from side lobe directions are called side-lobe artefacts (Figure 4). The most prominent side-lobe artefact is the arc-shaped specular artefact (Figure 4) that affects all beams at the shortest radial distance between the sonar and seabed (i.e., minimum slant range). This artefact is caused by the seabed at the range of the closest and thus earliest bottom return that interferes with measurements from the steered beams.

The stacked polar echograms were then exported as 3D point clouds (Latitude, Longitude, Depth, $S_v$) using a slant range that excludes the system-inherent specular and sidelobe artefacts (i.e., 0–95%) (Figure 4). As a result, only a relatively clean water column dataset inside the minimum slant range was retained.

The exported acoustic $S_v$ data was subsequently quality checked to remove wrongly georeferenced points with missing or out-of-bound coordinates (outside the BPNS; Marine Regions ID mrgrid 3293).

3D acoustic $S_v$ datasets from the water column are typically quite large. We collected gigabytes of data (163–1216 GB; Appendix A) despite the relatively short survey time

(ranging between 0.5 and 4 h) during each campaign. To efficiently work with these extensive point clouds, the data were ingested into "Entwine" (https://entwine.io) [87], a data library that organizes the point data in octrees to allow for spatial indexing at any particular location. Afterwards, the $S_v$ point cloud data were visually inspected in "Potree Viewer" (http://potree.org) [88].

#### 3.2.2. In-Situ Sensor Data

The raw LISST scattering intensities were converted to particle size distributions (in µL/L) using the "randomly shaped particle inversion model" (i.e., assuming natural particles with random shape) in the proprietary LISST-200X software (Version v1.14), as recommended by the manufacturer (Sequoia Scientific) when working in natural waters. The quality of the LISST datasets was checked using the following quality control metrics: positive depth values, stable transmitted laser power, laser reference values between 0.5 and 2, transmission values between 0.3 and 0.98. The latter indicates that there were no saturation problems. The raw OBS output was converted to Turbidity (in NTU) after applying an instrument-specific linear scaling constant that was predetermined by the producer (Sea-Bird Scientific) using a Formazin standard. The data quality of the OBS data was checked and outlier turbidity values (below 0 NTU) were removed. The OBS data were averaged in one second bins. The processed datasets from each sensor can be consulted on MDA [68]. For each campaign, an in situ sensor parameter table was created by merging all in situ sensor data using the timestamp of each sensor measurement. Finally, the measurements of the in situ sensors were georeferenced (XY coordinates) using the timestamp of the RVSS GPS system. These ship coordinates were logged continuously with the MBG-Tech RTK GPS system (UKKO GSS receiver with Septentrio technology). The depth values (Z coordinates) of the in situ measurements were retrieved from the depth sensor of the LISST. The 1-sec recordings of the combined in situ sensor data for each campaign can be found on GitHub [89].

Specifically for this study, we performed three additional processing steps with Python scripts [89]:

1. During the February and March 2021 campaigns, the raw LISST scattering intensity data displayed an abnormal spiky pattern, especially the first six rings, which is characteristic for optical misalignment (Appendix B). The TVC values, which normally reflect sizes between 1–500 µm, were therefore recalculated to 2.42–180 µm (February 2021 campaign) and 1–180 µm (March 2021 campaign).
2. Besides the particle concentration, particle sizes might also affect the scattering and absorption behavior, e.g., [17]. Hence, additional grain-size parameters were calculated based on the LISST's particle size distribution, including the mass division diameter D50 value. Finally, as flocculation in coastal areas is a transient process, subjected to varying turbulent shear stresses, the (multimodal) particle size distribution actually consists of different particle populations. Therefore, TVC (in µL/L) was recalculated for four size ranges: $TVC_{1–3\ \mu m}$, $TVC_{3–20\ \mu m}$, $TVC_{20–200\ \mu m}$, $TVC_{200–500\ \mu m}$, which were assumed to represent primary particles, flocculi, microflocs, and macroflocs, respectively [10,90].
3. As the depths of the acoustic $S_v$ datasets were corrected for the tides and transformed into depth LAT within SonarScope, the same tide correction and transformation needs to be applied to the in situ sensor track. Therefore, we calculated the corrected LAT water depths of the LISST using the continuous RTK signal of the ship, which was smoothed (Butterworth filter; low-pass normalized cut-off frequency: 1/200; order: 2).

### *3.3. Data Analysis*

We developed a workflow (Figure 5) in which we modeled an empirical relationship between in situ optical turbidity sensor data (TVC in µL/L from the LISST-200X; Turbidity in NTU from the OBS) and acoustic MBES ($S_v$ in dB) data recorded at the same time and location. This modeled relationship was then used to predict SPM in a 3D volume based on acoustic $S_v$ values from the water column.

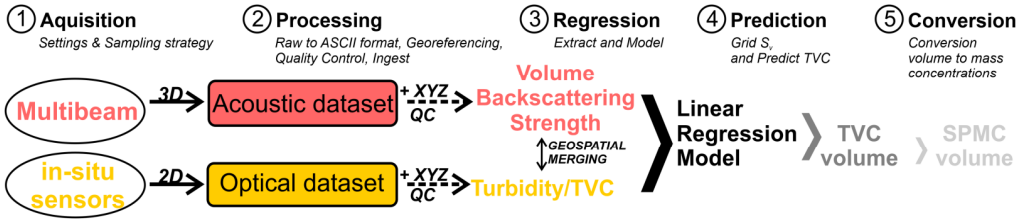


**Figure 5.** Overview of the workflow of the empirical approach used in this study to acquire and process acoustic and optical data in order to model Turbidity and TVC.

3.3.1. Regression and Prediction Analysis

An overview of the main steps of the regression and prediction analysis is provided in Figure 6. The analysis was performed using python scripts, which are available on GitHub [89].

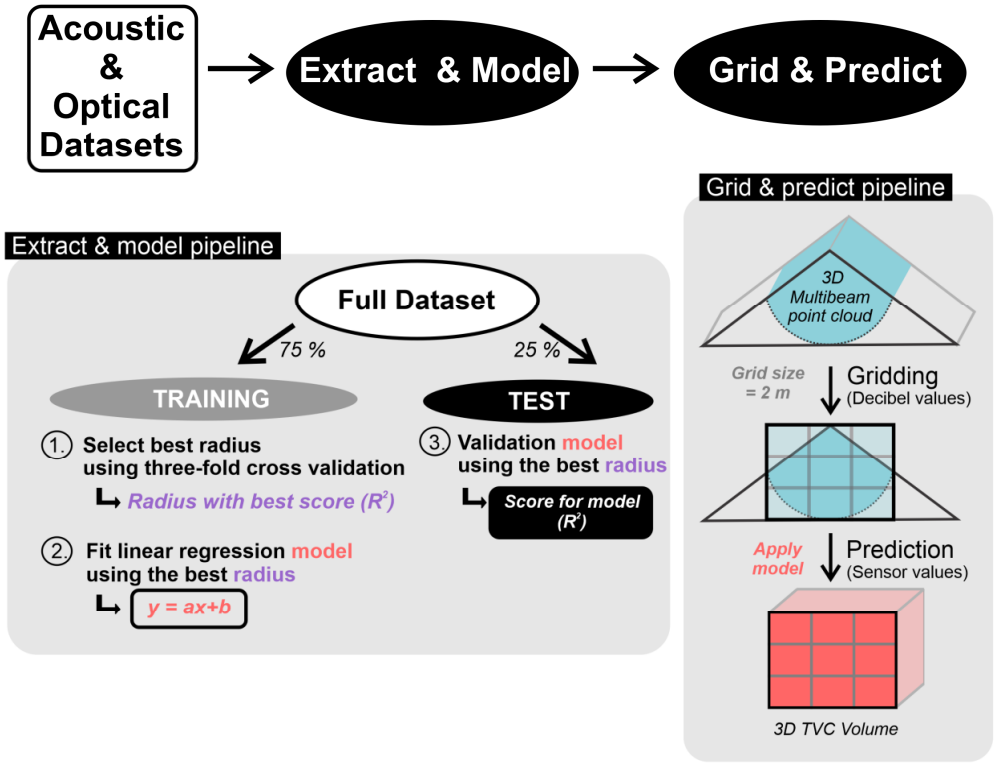


**Figure 6.** Overview of the main steps of the python code with specification of the extract and model, and grid and predict pipelines. CV = cross validation.

The regression analysis was performed on the georeferenced acoustic and optical data collected during multiple campaigns. This yields more variability in the dataset and reduces the risk of overfitting the model to single campaign conditions. The total size range of TVC was the same for three out of five campaigns (1–500 µm) and covers a large part of the size range of the SPM in the North Sea [90,91]. However, for the February and March 2021 campaigns (i.e., those with optical misalignment), the recalculated TVC reflects a more confined size range. Hence, TVC ($TVC_{1–500\ \mu m}$, $TVC_{1–3\ \mu m}$, $TVC_{3–20\ \mu m}$, $TVC_{20–200\ \mu m}$, $TVC_{200–500\ \mu m}$) was only modeled based on data from three campaigns (October 2020, May 2021, and July 2021). The modeling of optical turbidity (in NTU) was based on data from October 2020, February 2021, and March 2021, because during the May 2021 and July 2021 campaigns no OBS data were recorded (sensor malfunctioning).

As the volume of the water column representative for the in situ sensor measurements is smaller than the sampled volume of the MBES, all MBES points within a predefined

radius between 1, 2, 3, 4, and 5 m around each in situ sensor measurement were selected (3D spheres shown in Figure 7). These points were then averaged to be compared with the corresponding sensor values. The extraction and averaging of acoustic $S_v$ data was performed in PDAL (C++) (https://pdal.io) [92] and represents the most compute-intensive step of the presented workflow. Hence, PDAL pipelines were parallelized using Dask (https://dask.org/) [93], which is a Python library for parallel computation using dynamic task scheduling, rendering the computations scalable from a local machine to a cluster of machines. As we processed combined datasets from multiple campaigns (>2.5 TB), this required powerful computational resources. Therefore, we used the high-performance computer cluster facilities of the Flemish Supercomputer Center (VSC). We used a cluster of forty computers with four CPU cores and four gigabytes of RAM on each machine.

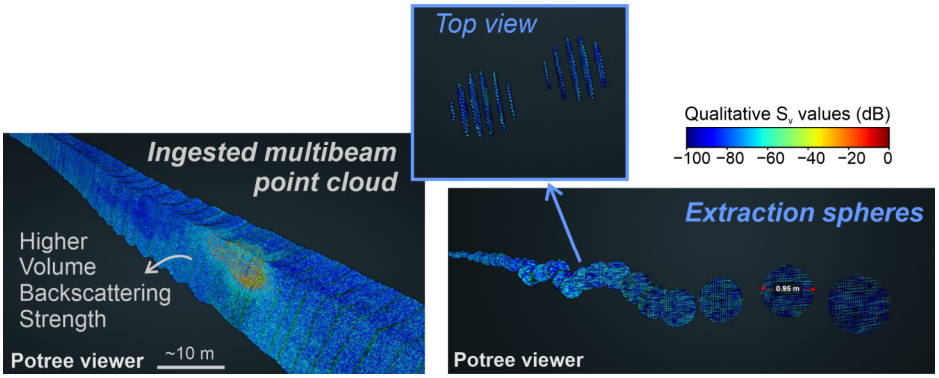


**Figure 7.** (**left**): 3D water column MBES point cloud visualization in Potree Viewer. (**right**): Extraction MBES spheres with predefined radius (here 0.5 m) around each in-situ sensor measurement. Data from October 2020 campaign.

The regression modeling was conducted in Python (Statsmodel library). The dataset was divided into randomly selected training (75%) and test (25%) datasets. The training dataset was used to select the best radius of the extraction sphere using a three-fold cross validation. Then, an Ordinarily Least Squares (OLS) regression model that assumes no uncertainties in the predictor variable (averages of $S_v$ values) was fit using this best radius. Finally, the linear regression model was validated with the test dataset using the best radius, yielding a scoring value (adjusted $R^2$) that indicates how well the model generalizes. The OLS regression modeling was performed on log10-transformed y-variables (in situ sensor measurements), because the unit of the predictor x-variable (decibels) is expressed on a logarithmic scale (base 10 logarithm). This approach is in accordance with Meslard et al. [22], Venditti et al. [47], and Fettweis et al. [94]. The y-variables consisted of the different size ranges of TVC ($TVC_{1–500\ \mu m}$, $TVC_{1–3\ \mu m}$, $TVC_{3–20\ \mu m}$, $TVC_{20–200\ \mu m}$, $TVC_{200–500\ \mu m}$) and optical turbidity.

The fitted regression model was then used to predict TVC based on the full 3D acoustic dataset. For this, a 3D grid with resolution of 2 m was created from the 3D MBES point cloud using a simple interpolation algorithm where each point that falls within a radius of 5 m of a raster cell center contributes to the raster value. The radius of 5 m was overall the best radius determined from cross validation. After the evaluation of the goodness-of-fit, the acoustic $S_v$ values for each point of the raster layers was transformed into (Log)TVC volumes using the generated linear regression model (with adj. $R^2 > 0.4$).

#### 3.3.2. Conversion to the Mass Concentrations

To compare between SPM measurements retrieved from different techniques, it is necessary to transform the TVC values measured by the LISST and predicted by the MBES into mass concentrations (SPMC; in mg/L) by multiplying with a density representative for the SPM mixture. However, determining the exact density of natural suspensions is difficult due to the heterogeneity of the SPM mixture [11,95]. As the density of all particles

in suspension decreases when the floc size increases (i.e., less than 100 kg/m$^3$ for organic macroflocs and more than 2650 kg/m$^3$ for mineral particles; [94]), mass concentrations were calculated following the fractal floc method (see Equation (1)). This approach assumes that big flocs consist of smaller primary particles, and it provides a mathematical framework to characterize sediment flocculation [96,97].

$$\rho_a = \rho_p \left[ \frac{d_p}{d_f} \right]^{3-F} \quad (1)$$

Several studies [11,95,98] followed this approach using data from their LISST-100X or LISST-100C to calculate floc size distributions (2.5–500 µm) by mass, assuming a primary particle size of $d_p$ = 2 µm and a fractal dimension of F = 2. Theoretically, this fractal dimension should fall between 1 and 3 depending on the packing of the flocs with F = 3 representing a solid spherical particle [96]. In practice, it is assumed that the fractal dimension F = 2 for marine and estuarine flocs [11,98]. In this study, we calculated the apparent floc density, $\rho_a$, for each size class between 2 and 500 µm (size class 4–36), with the floc diameter $d_f$ = median of each LISST size class and a primary particle density of $\rho_p$ = 2500 kg/m$^3$. As primary particles do not only consist of clusters of clay minerals, but also organic and calcareous particles, picophytoplankton, and heterotrophic bacteria [78,90], their density is estimated as the weighted sum of these different fractions, i.e., ~2500 kg/m$^3$ [7]. In contrast to previous studies that were conducted with a LISST-100, we used the LISST-200X, which measured particles smaller than 2 µm. For those smaller size classes (size class 1–3), we assumed an apparent density of $\rho_a$ = 2500 kg/m$^3$ [7], as they most likely constitute of primary particles. An error envelope for the apparent density was (artificially) created by varying the primary particle size between $d_p$ = 1–3 µm and the fractal dimension between F = 1.9–2.1, which are reasonable ranges for the Kwinte study area [7] (Appendix C). After calculating the densities for the 36 LISST size bins, we averaged the densities of size classes 1–36 ($\rho_{1–500\ \mu m}$), 1–6 ($\rho_{1–3\ \mu m}$), 7–17 ($\rho_{3–20\ \mu m}$), 18–31 ($\rho_{20–200\ \mu m}$), 32–36 ($\rho_{200–500\ \mu m}$) to match with the different TVC size ranges, i.e., $TVC_{1–500\ \mu m}$, $TVC_{1–3\ \mu m}$, $TVC_{3–20\ \mu m}$, $TVC_{20–200\ \mu m}$, $TVC_{200–500\ \mu m}$, respectively (Table 1). We then multiplied those average densities with the corresponding TVC to obtain an estimation of the mass concentration of the total suspended particulate matter ($SPMC_{1–500\ \mu m}$), primary particles ($SPMC_{1–3\ \mu m}$), flocculi ($SPMC_{3–20\ \mu m}$), microflocs ($SPMC_{20–200\ \mu m}$), and macroflocs ($SPMC_{200–500\ \mu m}$).

**Table 1.** Overview of the apparent density value ranges for North Sea SPM with different size ranges. The densities were calculated using the fractal method.

| Size Range (in µm) | North Sea SPM | Density $\rho_a$ (kg/m$^3$) | Lower Limit $\rho_a$ (kg/m$^3$) | Upper Limit $\rho_a$ (kg/m$^3$) |
|---|---|---|---|---|
| 1–3 | primary particles | 2329 | 1000 | 3175 |
| 3–20 | flocculi | 758 | 319 | 1213 |
| 20–200 | microflocs | 93 | 32 | 183 |
| 200–500 | macroflocs | 16 | 1 | 38 |
| 1–500 | SPM | 614 | 259 | 922 |

## 4. Results

### *4.1. Linear Regression Models*

We generated six linear regression models following the equation $Log_{10}(Y_i) = \alpha + \beta X + \varepsilon_i$ for different parameters (TVC size ranges and optical turbidity) (Table 2, Figure 8).

**Table 2.** Resulting parameters of the linear regression modeling for different TVC size ranges and optical turbidity using data from multiple campaigns combined.

| $Y_i$ | TVC (1–500 µm) | TVC (1–3 µm) | TVC (3–20 µm) | TVC (20–200 µm) | TVC (200–500 µm) | Optical Turbidity (NTU) |
|---|---|---|---|---|---|---|
| Observations n | 6529 | 784 | 6529 | 6529 | 6529 | 12024 |
| $\alpha$ | 3.635 | −6.499 | 4.134 | 4.134 | 1.524 | 5.979 |
| $\beta$ | 0.029 | −0.073 | 0.053 | 0.040 | 0.006 | 0.074 |
| Standard error $\alpha$ | 0.029 | 0.561 | 0.020 | 0.025 | 0.054 | 0.090 |
| Standard error $\beta$ | 0.000 | 0.008 | 0.000 | 0.000 | 0.001 | 0.001 |
| Standard error of regression $\varepsilon_i$ | 0.121 | 0.331 | 0.086 | 0.103 | 0.211 | 0.290 |
| $p$ value $\beta$ | 0.000 | 0.000 | 0.000 | 0.000 | 0.000 | 0.000 |
| Adjusted $R^2$ (test dataset) | 0.439 | 0.195 | 0.843 | 0.651 | 0.007 | 0.211 |
| Best radius (m) | 5 | 5 | 5 | 4 | 1 | 5 |

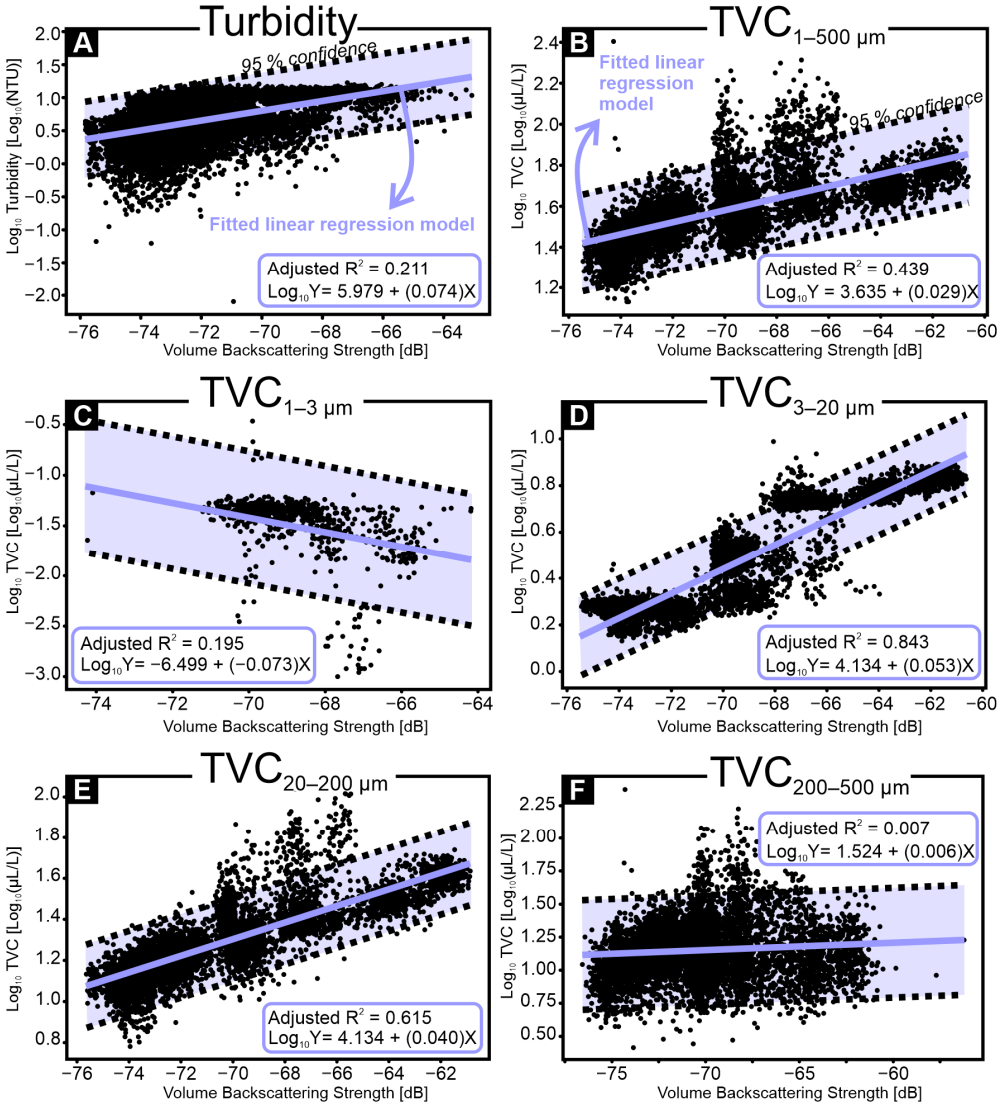


**Figure 8.** Linear regression models between $S_v$ (in dB), (**A**) log optical turbidity (in log NTU) and (**B**–**F**) different size ranges of log TVC (in log µL/L) ($TVC_{1–500\ µm}$, $TVC_{1–3\ µm}$, $TVC_{3–20\ µm}$, $TVC_{20–200\ µm}$, $TVC_{200–500\ µm}$) using data from multiple campaigns combined.

In order to examine the relations between $S_v$, log(TVC), and log(optical turbidity), the goodness-of-fit (adjusted $R^2$) and the significance of the x-coefficient (β) are computed. The adjusted $R^2$ shows how well $S_v$ explains the variance of the modeled in situ parameters ($TVC_{1–500\ \mu m}$, $TVC_{1–3\ \mu m}$, $TVC_{3–20\ \mu m}$, $TVC_{20–200\ \mu m}$, $TVC_{200–500\ \mu m}$, optical turbidity). A clear difference in adjusted $R^2$ is observed between different input parameters, ranging from 0% ($TVC_{200–500\ \mu m}$) to 84% ($TVC_{3–20\ \mu m}$) of the variance that is explained by $S_v$ (Table 2). The t-tests shows that the coefficients of the x-variable ($S_v$) are statistically highly significant for each model ($p$-value < 0.0001), even for those models with the lowest goodness-of-fit.

### 4.2. SPMC Volumes

The $TVC_{1–500\ \mu m}$ linear regression model was used to convert the gridded 3D $S_v$ volumes of each campaign into a 3D grid, which displays the mean mass concentrations of the total suspended particulate matter ($SPMC_{1–500\ \mu m}$). To obtain these SPMC estimations, the densities of SPM (Table 1) were used.

The converted mean SPMC volumes of each campaign can be consulted in Zenodo [99]. Investigation of these plots reveals clear spatiotemporal variability in the BPNS. For example, during the March 2021 campaign, we detected a remarkable layer with high $S_v$ and SPMC values in the water column at −14 m LAT around noon (Figure 9). Eventually, this layer slowly descended and eventually disappeared around 2 pm. The spatiotemporal aspect of this feature was captured by the 3D SPM grid. The reason why the layer is not "visible" in the eastern part of grid is because we surveyed from West to East, so the layer was already gone when we surveyed the eastern part of the survey area. This phenomenon is discussed in more detail in Section 6.4.

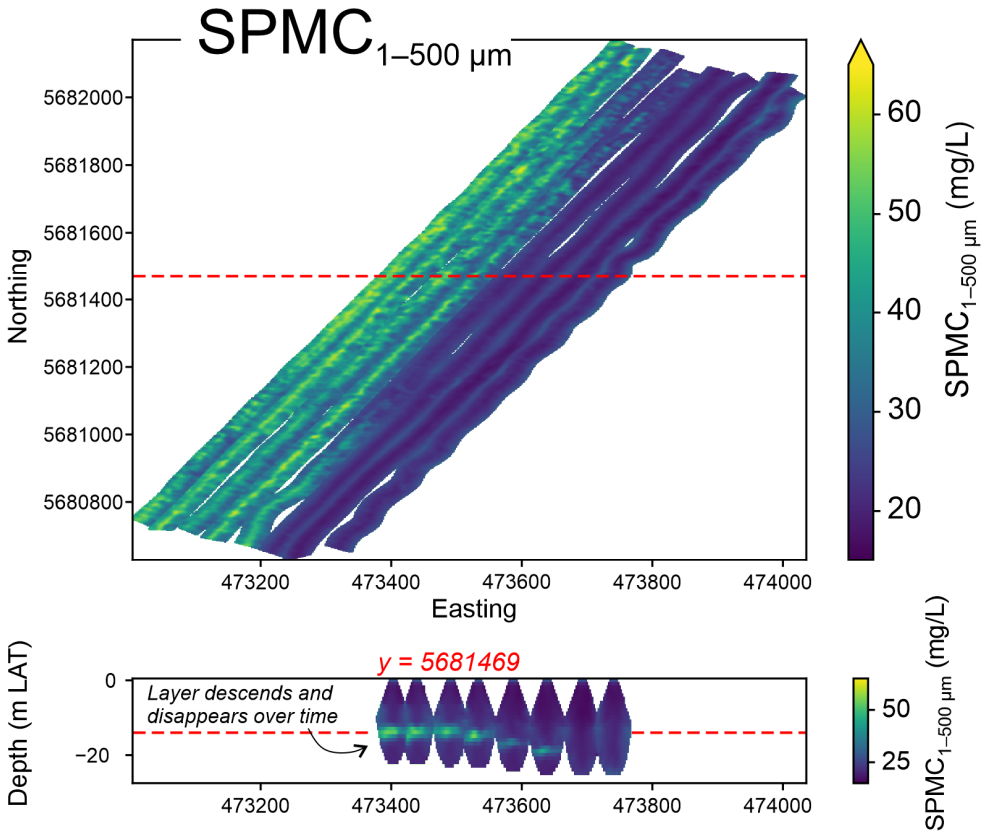


**Figure 9.** Horizontal slice at −14 m LAT depth (**top**) and a vertical cutaway (**bottom**) through a 3D volume of the converted mean mass concentration of total suspended particulate matter ($SPMC_{1–500\ \mu m}$) showing clear temporal variability of SPM within the water column. Data from the March 2021 campaign. Coordinates are given in UTM (zone 31 N). The red dotted line indicates the location of the vertical cutaway (top) and the depth of the horizontal slice (bottom).

## 5. Discussion

### *5.1. In Situ Sensor Datasets*

The developed linear regression models (Figure 8) are presumably not generalized relationships, as they are inherently bound to the specific SPM properties of the days and locations on which the sensor data was gathered. Therefore, it is useful to first describe these specific SPM properties (optical turbidity, TVC, and particle size distribution) by using the collected LISST and OBS datasets. The ranges of SPM properties are not normally distributed; hence, we report the median and the interquartile ranges (IQR) (Figure 10) of these distributions.

Due to optical misalignment of the LISST-200X in the February and March 2021 campaigns, the modeling of TVC was based on data from campaigns in October 2020, May 2021, and July 2021, coinciding with summer/autumn conditions. In contrast, because no optical turbidity data were recorded during the May 2021 and July 2021 campaigns, the modeling of optical turbidity was based on data from October 2020, February 2021, and March 2021, coinciding with autumn/winter conditions. Although it is difficult to compare these datasets with each other, they provide an insight into the seasonal SPM properties of the study area.

The observed median Turbidity (4.3 NTU) in autumn/winter and the TVC (35.2 µL/L) and D50 (156.9 µm) in summer/autumn (Figure 10) are in line with other studies in the BPNS that present data from comparable low turbidity offshore locations, e.g., W05 and W08 (Figure 1) [9,11]. The particles are larger in summer because biological activity during summer produces fresh adhesive organic material, which results in enhanced flocculation. As the flocs' sizes increase, the settling velocities increases. Subsequently, the SPM concentration and turbidity decrease. In contrast, SPM and turbidity increase during winter [11].

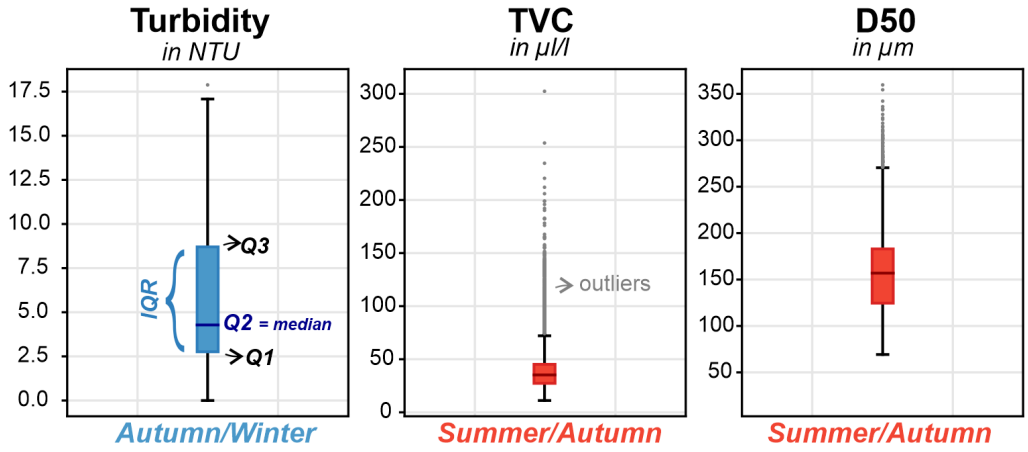


**Figure 10.** In situ sensor summary box plots of ranges of Turbidity (derived from OBS), Total Volume concentration, and D50 (derived from LISST), averaged over all depths. OBS measurements were only available for the "autumn/winter" months (October 2020, February 2021, March 2021), while LISST measurements were only retained for the "summer/autumn" (October 2020, May 2021, July 2021) months. Box plots parameters: outliers, Q1−1.5 × IQR, Q1 25%, Q2 50%, Q3 75%, Q3 + 1.5 × IQR, outliers.

The particle size distribution in summer/autumn is multimodal (with peaks around 10, 80, and 250 µm) (Figure 11). This observation is in accordance with reported multimodal particle size distributions (with peaks around 10, 50–100, and 300 µm) in stations W05 and W08 in early autumn [11]. In terms of volume concentrations, (small) macroflocs are most abundant, followed by microflocs and flocculi (Figure 11).

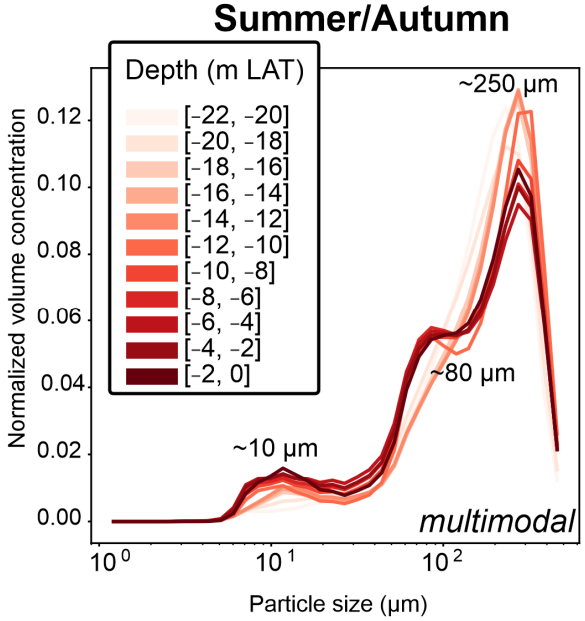


**Figure 11.** PSD plots (derived from the LISST-200X), binned every 2 m, for the "summer/autumn" (October 2020, May 2021, July 2021) dataset. The volume concentration is normalized by dividing the values with the total volume concentration.

### *5.2. Evaluation of the Linear Regression Models*

This evaluation discusses the differences between the developed linear regression models (Figure 8, Table 2), which describe the relation between acoustic $S_v$ and the in situ parameters. It should be noted that the models of optical turbidity (Figure 8A) and TVC (Figure 8B–F) are based on different datasets and that a comparison of those is therefore not straightforward.

In the optical turbidity regression model (n = 12024), acoustic $S_v$ explains only a small part of the variability (adj. $R^2$ = 0.211) (Figure 8A). For that reason, we have discarded this model for further analysis. The low level of correlation may be explained by (a combination of) different reasons. First, we hypothesize that the significant difference in sensitivity between the OBS and the MBES sensors (as mentioned in Section 3.1.3) might provide a reason for the weak correlation. In areas with relatively low SPM concentrations, such as the investigated Kwinte and Westdiep areas [7], OBS sensors are more sensitive to fine-grained mud particles [17], while the interaction between an acoustic pulse and particles is optimal for coarse-grained high-density sandy particles [73]. Furthermore, the optical turbidity model was based on data from winter months. In winter, a relatively higher abundances of fines are present, which might be favorable for particle detection by OBS sensors, while these grain sizes are less optimal for the 400 kHz MBES system (see Section 3.1.3). Second, during our campaigns we only encountered a small range in optical turbidity values in the Kwinte area. More campaigns in other areas and seasons will increase the measured optical turbidity range, which might be beneficial for the goodness-of-fit of the linear regression model. Third, there is a difference in sampling volume between the optical and acoustic measurements. The OBS measurements represent a small measurement volume (in the order of ~$cm^3$). Hence these optical measurements are expected to exhibit more variability when compared to the averaged measurements within the large multibeam spheres (4–500 $m^3$). This difference in sampling volume could affect the correlation. However, the sampled volumes of the OBS and LISST sensors are very similar, so this difference in measurement volume alone cannot explain the weak relationship between $S_v$ and optical turbidity.

Finally, the low level of correlation can be due to the lack of frequent sensor calibration, which detects and corrects for instrument drift over time [94].

The clear difference in adj. $R^2$ values between $S_v$ and the different size ranges of TVC could be caused by the acoustic sensitivity towards each of these classes. Acoustic $S_v$ explains a high proportion of the variance in the LISST-derived volume concentration of particles with a size range between 1 and 500 µm (adj. $R^2$ $TVC_{1–500\ \mu m}$ = 0.439) (Figure 8B). The goodness-of-fit is even better when confining the default total size range of the LISST to 3 to 20 µm (adj. $R^2$ $TVC_{3–20\ \mu m}$ = 0.843) (Figure 8D) and 20 to 200 µm (adj. $R^2$ $TVC_{20–200\ \mu m}$ = 0.651) (Figure 8E). These confined size ranges overlap with the sizes of flocculi and microflocs in the North Sea. The size range between 20 and 200 µm could also match with sand (>63 µm) particles in suspension; however, these are mostly found near-bed [9] where none of the in situ measurements were conducted and no MBES water column data were retained (cut-off 95% to exclude side lobes). Since flocs are the most abundant (in terms of volume concentrations; Figure 11), it is surprising that the adj. $R^2$ values are higher for smaller size classes because the MBES 400 kHz operating frequency provides in theory optimal acoustic scattering for larger grain sizes (~1200 µm, see Section 3.1.3). However, the particles in each size class might have specific particle properties (such as density, shape, refractive index, surface roughness), which also affect the scattering and absorption behavior besides the size criterium (Haalboom et al. [17]; and the references therein). For example, if we are correct to assume that the calculated density of the particles in the $TVC_{3–20\ \mu m}$ and $TVC_{20–200\ \mu m}$ class is relatively higher than the density of the (flocculated) particles in the $TVC_{200–500\ \mu m}$ class then the higher density probably causes the acoustics to be more responsive compared to larger particles with lower densities. Furthermore, the modeling of TVC was based on data from campaigns in October 2020, May 2021, and July 2021, coinciding with summer/autumn conditions. Due to the presence of algal blooms in spring and early summer, more flocculation occurs during those periods [11]. Although the acoustic response of non-cohesive sandy sediments is relatively well understood through decades of studies (see review of Thorne and Hurther [34]; and the references therein), only recent attempts were made to focus on cohesive sediments and to quantify the impact of flocculation on the acoustic scattering [35,41,42,100–103]. Several of these studies demonstrated that a suspension of flocculated particles can lead to optimal conditions for acoustic detection. This is not only because of the larger floc size, but also its composition affects the scattering behavior and can result in a "scattering reinforcing" effect. First, this is because flocculation apparently does not affect the attenuation of sound [103]. Second, this is because scattering of a suspension of flocculated particles is higher compared to a suspension of non-flocculated particles with the same concentration and primary particles [41,102]. According to Thorne et al. [42], Pedocchi and Mosquera [103], and Vincent and MacDonald [104], flocs scatter sound as if they were single elastic or fluid spheres, causing enhanced scattering compared to primary particles. These abovementioned hypotheses might explain the high goodness-of-fit for the $TVC_{20–200\ \mu m}$ (microflocs) model, but the reason for the very high fit of the $TVC_{3–20\ \mu m}$ (flocculi) model remains unclear. The plot for the LISST size range between 3–20 µm (Figure 8D) shows a clustered distribution of the datapoints. We thus believe that the correlation in this size range requires further investigation despite the computed high goodness-of-fit.

There is a weak correlation between acoustic $S_v$ and the volume concentrations of the smallest (adj. $R^2$ $TVC_{1–3\ \mu m}$ = 0.195) (Figure 8C) and largest (adj. $R^2$ $TVC_{200–500\ \mu m}$ = 0.0067) (Figure 8F) size ranges, which correspond to the size range of primary particles and macroflocs in the North Sea, respectively. The MBES system in the 400 kHz mode is very insensitive to the smallest size ranges, because the $S_v$ of grain sizes with a diameter of ~3 µm is already ~104 dB less compared to the optimal grain size of 1200 µm (see Section 3.1.3). Furthermore, their concentration was probably too low to cause a significant increase in the MBES signal. Indeed, these primary particles were also less commonly detected by the LISST, resulting in substantially lower number of observations for the $TVC_{1–3\ \mu m}$-model (n = 784) compared to the other models (n = 6529).

Macroflocs, which are abundant during spring and summer (dataset TVC models), are most likely to be detected by the 400 kHz operating frequency of the MBES system,

solely based on their large size (~250 µm) and their flocculated internal structure e.g., [103]. The low adj. $R^2$ value might then be explained by the fact that for macroflocs, composition, rather than size or abundance, controls the acoustic $S_v$. We hypothesize that the macroflocs in our dataset consist mostly of jelly material, so the "scattering reinforcing" effect of the floc components is likely negligible. Another reason could be that for macroflocs with low densities of 15 kg/m$^3$ (Table 1), the impedance contrast between the particles and the sea water is so low that the sensitivity of the acoustic sensors is significantly reduced.

### *5.3. Evaluation of the SPMC Volumes*

The acoustically measured 3D volumes of converted SPMC in this study (available in Zenodo [99]) make it possible to discuss the SPMC ranges for an array of depth intervals in the water column (depth variability) over a large area (lateral variability). In order to ensure comparability with other studies and sensors, we only discuss the converted mass concentrations of the total suspended particulate matter (i.e., $SPMC_{1–500\ \mu m}$).

In the Kwinte area, SPMC values fluctuate around 25 mg/L and SPMC variability is more pronounced with depth compared to the lateral variability (Figure 12). This is testified to by the SPMC increase towards the water surface (>25 mg/L), which is larger than the lateral variability in the study area. Only a few depth intervals (e.g., −10 m in February 2021 and −15 m in March 2021) on the density plots (Figure 12) display larger lateral variability, which is still below the increase of SPMC towards the water surface. The shallower Westdiep area shows almost no SPM variability with depth, but does display relatively large lateral variability below the surface water (values between 25–50 mg/L). In both the Kwinte and Westdiep areas, SPMC ranges are narrow in the first meters of the water column, while there is more (lateral) variability below the surface water.

The presented SPMC ranges are within the limits of the reported yearly averages of vertically averaged SPMC in the study area, i.e., between 10 and 50 mg/L [7]. However, the comparison of the converted SPMC datasets with previous SPM studies in the same area should be interpreted with care because the sampling strategy in this study is inherently different in both time and space from the tidal cycle measurements from a vessel or long-term measurements with tripods. Furthermore, previous studies show that SPMC values are lower in spring/summer than in autumn/winter [7,31,105,106]. Opposed to the results of these longer-term measurements that are averaged over several tidal cycles, we do not observe a distinct seasonal variation in the converted SPMC in the Kwinte area. However, our data lacks this longer term imprint, because this study focused on the development of a new methodology rather than the assessment of seasonal SPM variations. In the future, it would be interesting to apply the new methodology for longer term monitoring by conducting multiple surveys in different seasons during the year.

SPMC was also measured from Niskin water samples during each campaign, with the exception of the October 2020 campaign (Figure 12). Caution should be taken when comparing the measured and converted SPMC since the sampling location might be just outside the converted SPMC volumes and there is a time delay (minutes to hours) between the water sampling and the acoustic and optical measurements. The measured SPMC values show a lot more variability with depth than the converted SPMC ranges, but this is reasonable as the converted SPMC data are gridded and thus represent averages over a larger volume. Nevertheless, they are in the same order of magnitude (Figure 12), providing additional proof that our converted SPMC values are trustworthy.

### *5.4. Evaluation of the Sources of Uncertainty and Error*

In this study, an empirical approach was used for the first time to predict TVC from acoustic $S_v$ and to estimate SPM over a 3D volume in an uncontrolled environment. The MBES-derived TVC and converted SPM volumes are the result of several acquisition, processing, and modeling steps (Figure 5), which all contribute (randomly and systematic) to the overall estimated SPM uncertainties. Providing an exact review of the error propaga-

tion is beyond the scope of this study. Nevertheless, in Appendix C we try to provide an overview of the errors introduced by the statistical operations (Figure 6).

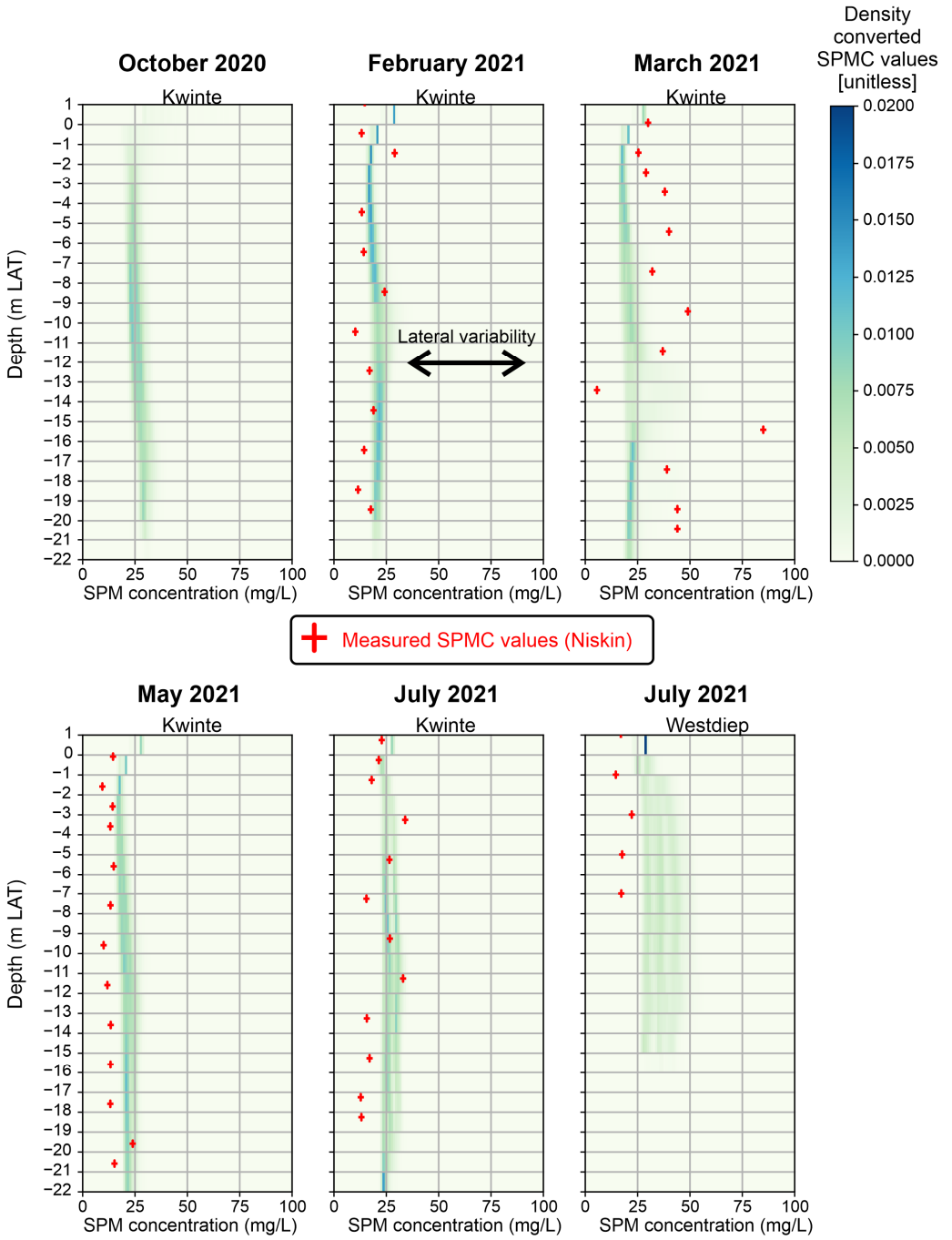


**Figure 12.** Overview of the probabilistic densities of the converted mean $SPMC_{1-500\ \mu m}$ for different depths (in m LAT), showing the SPMC ranges with depth for different seasons and areas. The measured SPMC from Niskin water samples (at a fixed location) was provided for comparison. The depth was cut off at 1 m LAT because no co-located MBES and in situ sensor data were collected above this depth.

## 6. Lessons Learned and Outlook

In this study, we learned several valuable lessons that will help us move towards operational use of MBES as a common tool for SPM monitoring in the future.

### *6.1. Survey Strategy*

To ensure comparability of acoustic datasets over different campaigns, between different MBES systems, and between different beams, MBES calibration is necessary [54,83,84,107]. For example, stronger $S_v$ values in the center beams were noticed compared to the outer beams (Figure 9), probably due to the lack of inter-beam calibration. We assumed that the calibration constant was uniform for different surveys and for each beam. However, small errors between surveys and between beams will increase the uncertainty on the empirical relationship. Hence, in future studies we recommend taking into account these (absolute and relative) MBES-specific corrections.

The conversion of TVC to SPMC is ideally done by multiplying with a density value derived from field calibrations after collection of concurrent stationary water samples and sensor measurements [14,94,108]. However, during the campaigns, no concurrent LISST and SPMC data were collected. Therefore, density values were calculated using a mathematical approach based on the fractal floc method [96,97]. For future studies, we recommend a field calibration of the LISST to make the conversion of the volume to mass concentrations more reliable.

As a result of the sampling strategy, the in situ sensors make undulating movements behind the boat, which may induce additional uncertainties. Depending on the current direction and velocity, an offset of a few tens of meters in the X and Y directions between the transducer and the towed sensors may be present. This offset is two orders of magnitude higher than the positional accuracy of the GPS system (a few cm given the RTK corrections). Although the offset was not considered for the correlation, this should not pose an issue in the Kwinte area where the SPMC variability with depth is more important than the lateral variability (Figure 12). This vertical variability was measured very precisely with the depth sensor of the LISST. In the future, more accurate positioning data could be obtained using underwater positioning systems.

### *6.2. MBES Water Column Processing*

Several important lessons were learned regarding the processing of MBES water column data. First, we realized that the available software lacks proficient processing capabilities. Commercially available packages mainly focus on visualization of pings or a limited amount of scatterers in the water column, while the few processing software packages that allow quantitative processing of acoustic $S_v$ from the water column involve inflexible and non-transparent workflows. Therefore, we strongly recommend the development of a powerful, well-documented, open-access processing software.

Second, water column MBES data is noisy. Noise can be minimized as much as possible by selective settings (single sector mode avoids multi-sector artefacts; Supplementary Document S1), acquisition strategy (switching off all other echosounders to avoid interferences; sailing in a straight line at low constant speed), and processing (a slant range between 0–95% excludes the noisy sidelobes; Supplementary Document S3). Despite these efforts, it is probable that there are still some artefacts present in the MBES data. These remaining artefacts could not be filtered because the processing software (SonarScope) does not allow us to delete individual erroneous bins within the polar echogram. Instead, the complete polar echogram needs to be deleted after visual inspection of every ping, which is a time-consuming process. Therefore, we also recommend the development of machine learning approaches for target detection on polar echograms. These automatization tools can then be used to recognize and delete water column artefacts in a more targeted manner. Using such an automated editing approach in combination with manual editing was also recommended by Urban et al. [58]. Finally, raw MBES datasets from the water column are very large (several gigabytes per hour, depending on the ping rate; Appendix A), which hampers fast processing in SonarScope afterwards. The processing of small datasets (<50 GB) was feasible from standard workstations, but the processing of larger datasets (>50 GB) was very time-consuming. In addition to capable software, significant processing power is thus required to handle these datasets.

### *6.3. Statistical Modeling*

The main limitation of our linear regression models is that they are inherently bound to the properties of the coastal waters in the BPNS and the used MBES system. At best they are extendable to comparable regions (Table 2) with the same system and settings. Therefore, these models should not be used as generalized relationships in other water types, for example the open ocean. The linear regression models from this paper can be readily used in the BPNS by accepting that the MBES-derived SPMC measurements are probably slightly less accurate for datasets with other properties than the datasets from this study (in the Kwinte/Westdiep area in the summer season). We recommend testing the empirical approach in a wide variety of environments to develop a set of relationships for specific waterbodies and climate conditions. Alternatively, campaign-specific empirical relationships can be developed, but this will be more time-consuming. Such a model appropriate for the suspension at that time can be created by first performing stationary measurements with the collection of concurrent acoustic, optical, and water samples (in close proximity to the expected ensonified water volume).

In this study, a linear relationship between acoustic $S_v$ and the in situ parameters was assumed in order to easily predict optical turbidity or TVC based on acoustic $S_v$. However, the acoustic scattering behavior of natural suspensions is complex e.g., [35,109] and the prediction of SPMC is in fact a multivariate problem. Hence, we suggest exploring how to optimize the relationship between acoustic $S_v$ and SPM properties (particle size, shape, etc.) with more sophisticated statistical and/or machine learning approaches.

Finally, MBES acoustic $S_v$ datasets are very large (Appendix A), which hampers straightforward correlation with the in situ sensor datasets. Hence, the statistical modeling of large datasets (>1 TB), especially when combining data from multiple campaigns (>2.5 TB), requires high-performance computing facilities.

### *6.4. Target Ambiguity*

At the moment, it is still difficult to distinguish between different types of targets (sediment, plankton, flocs, bubbles, fish, etc.) that are captured by the MBES. The interpretation of the acoustic signal is not straightforward because acoustic $S_v$ is not only a function of SPM concentration, but also the type (biological-dominated versus sedimentological-dominated) and size of particles or aggregates. Furthermore, the backscatter response to different particle sizes is dependent on the operating frequency [110].

As multiple optical and acoustic sensors have different particle types and size sensitivities, a multi-sensor approach might be key in solving the issue of target ambiguity. During the March 2021 campaign, we detected a remarkable layer with high $S_v$ and SPMC values in the water column at −14 m LAT around noon (Figure 9). The SPM concentrations determined from the Niskin water samples (in station LW215; Figure 1) show a clear increase from −13 (5.6 mg/L) to −15 (85 mg/L) m LAT depth (Figure 12), while the other optical in-situ sensors (LISST, OBS) do not detect this layer [68]. The advantage of using MBES data is that it allows visual inspection of the geometry of features in polar and longitudinal echograms, which can then help to understand their nature. We reckon that based on the layer's morphology and its mobility and the size of the targets within the layer (Supplementary Video S1), it most likely represented a school of small fish such as sprat (8–16 cm) [56,111], which can perform vertical migrations on a diurnal basis [112,113]. Furthermore, these small planktivorous fish were possibly attracted by zooplankton that concentrated around the subtle pycnocline where nutrient-rich aggregates are typically accumulated [114]. The presence of zooplankton might then explain the higher SPM concentration measurements, but it remains unclear why this SPM type was not captured by the optical sensors. Visual inspection of the echograms can thus help solve the issue of target ambiguity, but this process is very time consuming. Automation using machine learning approaches to cluster different acoustic signals and evaluate if they can be linked to different targets could be a faster solution.

Another solution would be the recording of the MBES data in multiple frequencies. The relative differences in target response [115] might help to discriminate targets, particle sizes, and maybe even SPM types in the future. Furthermore, multifrequency MBES measurements may make it possible to estimate both size distribution and concentration by using scattering models and robust inversion methods [35,110]. Unfortunately, the multifrequency recording option is not widely available yet on ships. Moreover, using MBES in multifrequency mode would ideally require absolute calibration for all frequencies, which is costly and time-consuming [53,54,83,84]. If absolute calibration is not feasible, the relative signal variation within each frequency may still improve the ability to distinguish targets and/or particle sizes.

Finally, we suggest better monitoring of the varying SPM properties by collecting more abundant water samples (and by applying microscopy and imaging tools on those samples), or by collecting underwater cameras that capture particles in situ.

In conclusion, we need more studies tackling the problem of target ambiguity. During acquisition, we recommend a multi-frequency, multi-sensor approach to discriminate between different types of scatterers in the water column and their wide spectrum of sizes.

## 7. Conclusions

In this study, we developed an innovative empirical methodology to convert acoustic $S_v$ data from the water column to quantitative 3D SPM information. We created the first 3D SPM maps of areas inside the BPNS, which is an important step towards improving our understanding of dynamic natural and anthropogenic hydro-sedimentary processes in that region. The large spatial coverage of the 3D SPM maps allows us to observe SPM-related phenomena in the water column that otherwise would be missed by traditional monitoring approaches. This estimation of SPM over a 3D volume in a natural environment shows the potential of MBES for future monitoring purposes in scientific and industrial sectors. This is particularly interesting because multibeam systems are included as standard equipment on many ships for use in bathymetric surveys.

This study showed that SPM monitoring using MBES systems is a valuable method next to the more conventional monitoring approaches. Depending on the scope of the study, satellite remote sensing is still recommended for monitoring large areas of surface waters. Moreover, traditional optical (LISST, OBS) and acoustic (ADCP, ABS) instruments are preferred for stationary measurements in the water column. Single beam systems and ADCPs are powerful tools for transects. However, MBES measurements have the advantage of estimating SPM over a much larger volume in the water column.

This study helped to expand the possibilities for using multibeam sonars as an SPM monitoring tool in the future. However, methodological improvements are still required to unlock the full potential of MBES for SPM monitoring. Possible future directions worth being investigated are the implementation of multifrequency approaches, low-cost calibration during acquisition, and faster automated processing.

**Supplementary Materials:** The following supporting information can be downloaded at: https://www.mdpi.com/article/10.3390/rs15204918/s1: Document S1: Timbers protocol for EM2040 SIS settings, Document S2: Timbers protocol for LISST-200X settings and deployment, Document S3: Timbers protocol for water column backscatter processing in SonarScope, Video S1: Video of a school of fish in EM2040 multibeam water column data from March 2021 in the Kwinte Area.

**Author Contributions:** Conceptualization, N.P., T.C. and T.V.; Data curation, N.P.; Formal analysis, N.P. and T.C.; Funding acquisition, M.D.R. and T.V.; Investigation, N.P. and T.C.; Methodology, N.P., A.O. and T.V.; Project administration, M.D.R. and T.V.; Resources, M.D.R. and T.V.; Software, T.C., M.R. and K.D.; Supervision, M.R., K.D. and T.V.; Validation, N.P., T.C. and T.V.; Visualization, N.P.; Writing—original draft, N.P. and T.V.; Writing—review and editing, N.P., A.O., M.R., M.D.R. and P.U. All authors have read and agreed to the published version of the manuscript.

**Funding:** This research was conducted in the framework of the TIMBERS project (grant number SR/00/381) and the STURMAPSS dissemination project (grant number SR/L9/221), both funded by

the Belgian Federal Science Policy Office BELSPO (Stereo III program). Furthermore, the paper was revised during the BELSPO-funded TURBEAMS project (grant number RV/21/TURBEAMS). The APC was funded by Flanders Marine Institute.

**Data Availability Statement:** The raw ASCII MBES datasets are not publicly available due to restrictions in file size, but are available upon request from the corresponding author. The raw in-situ sensor datasets are available on the VLIZ Marine Data Archive (https://doi.org/10.14284/572). The Python scripts (https://doi.org/10.5281/zenodo.8423005) and datasets (https://doi.org/10.5281/zenodo.8013207) that support the findings of this study will be openly available in Zenodo and GitHub.

**Acknowledgments:** This research was conducted in the framework of the TIMBERS project (in collaboration with VITO and the University of Connecticut), the STURMAPSS (dissemination) project and the TURBEAMS project (in collaboration with Ghent University, RBINS and FPS Economy). All projects were funded by the Belgian Federal Science Policy Office BELSPO. We would like to thank the TIMBERS partners (R. Moelans, E. Knaeps, L. De Keukelaere, H. Dierssen, D. Iordache), the TIMBERS steering committee (S. Garaba, M. Chami, M. Roche, S. Simmons) and J-C. Schyns and J. Vandenabeele for the fruitful discussions and their constructive feedback. We appreciate the assistance of the Vloot Staff during the campaigns with the RV Simon Stevin. The resources and services used in this work were provided by the VSC (Flemish Supercomputer Center), funded by the Research Foundation-Flanders (FWO) and the Flemish Government. Filtration and gravimetric analyses of the water samples were performed by the Flanders Environment Agency (VMM). This work was supported by data and infrastructure provided by VLIZ as part of the Flemish contribution to LifeWatch. We also want to acknowledge the Infrastructure department of Flanders Marine Institute and especially the technical support from D. Vansteenwegen, M. T'Jampens, and R. Develter.

**Conflicts of Interest:** The authors declare no conflict of interest. The funding sponsors had no role in the design of the study; in the collection, analyses or interpretation of data; in the writing of the manuscript; or in the decision to publish the results.

## Appendix A

**Table A1.** Overview of the recorded and processed MBES lines, the used in situ sensors, and the survey area (and sampling station) for each campaign (campaign number in italic).

| CAMPAIGNS | DATE | RAW MBES DATA | PROCESSED MBES DATA | IN-SITU SENSOR TOOLBOX | SURVEY AREA (STATIONS) |
|---|---|---|---|---|---|
| **OCTOBER 2020** *20-690* | 5 October 2020 | 13.2 GB | 163 GB | LISST, OBS | Kwinte |
| **FEBRUARY 2021** *21-092* | 4 February 2021 | 90.4 GB | 1216 GB | LISST, (OBS), Niskin | Kwinte (LW215) |
| **MARCH 2021** *21-160* | 1 March 2021 | 62.7 GB | 594 GB | LISST, OBS, Niskin | Kwinte (LW215) |
| **MAY 2021** *21-430* | 28 May 2021 | 33.3 GB | 382 GB | LISST, Niskin | Kwinte (LW215) |
| **JULY 2021** *21-550* | 9 July 2021 | 23.3 GB | 188 GB | LISST, Niskin | Kwinte (LW215) Westdiep (Timbers 15) |

## Appendix B

During the February and March 2021 campaigns, the raw LISST-200X scattering intensity data displayed an abnormal spiky pattern, especially the first six rings, which is characteristic for optical misalignment. As a result, the outer size classes are susceptible to errors, leading to false appearance of small and large particles (Figure A1). We therefore decided to discard the corresponding erroneous six upper size classes, which is a common strategy to deal with the highly variable accuracy of the outer size classes [14,116]. Further inspection of the particle size distribution of the February 2021 campaign also showed a clear increase in the lower four size classes. This faulty "rising tail" might point to an overestimation of fine particles due to inaccuracy of the LISST instrument or unwanted shape and composition effects [78,117]. Hence, these four lower size classes were discarded. Then

the TVC values, which normally reflects a size range between 1–500 µm, were recalculated to 2.42–180 µm (February 2021 campaign) and 1–180 µm (March 2021 campaign).

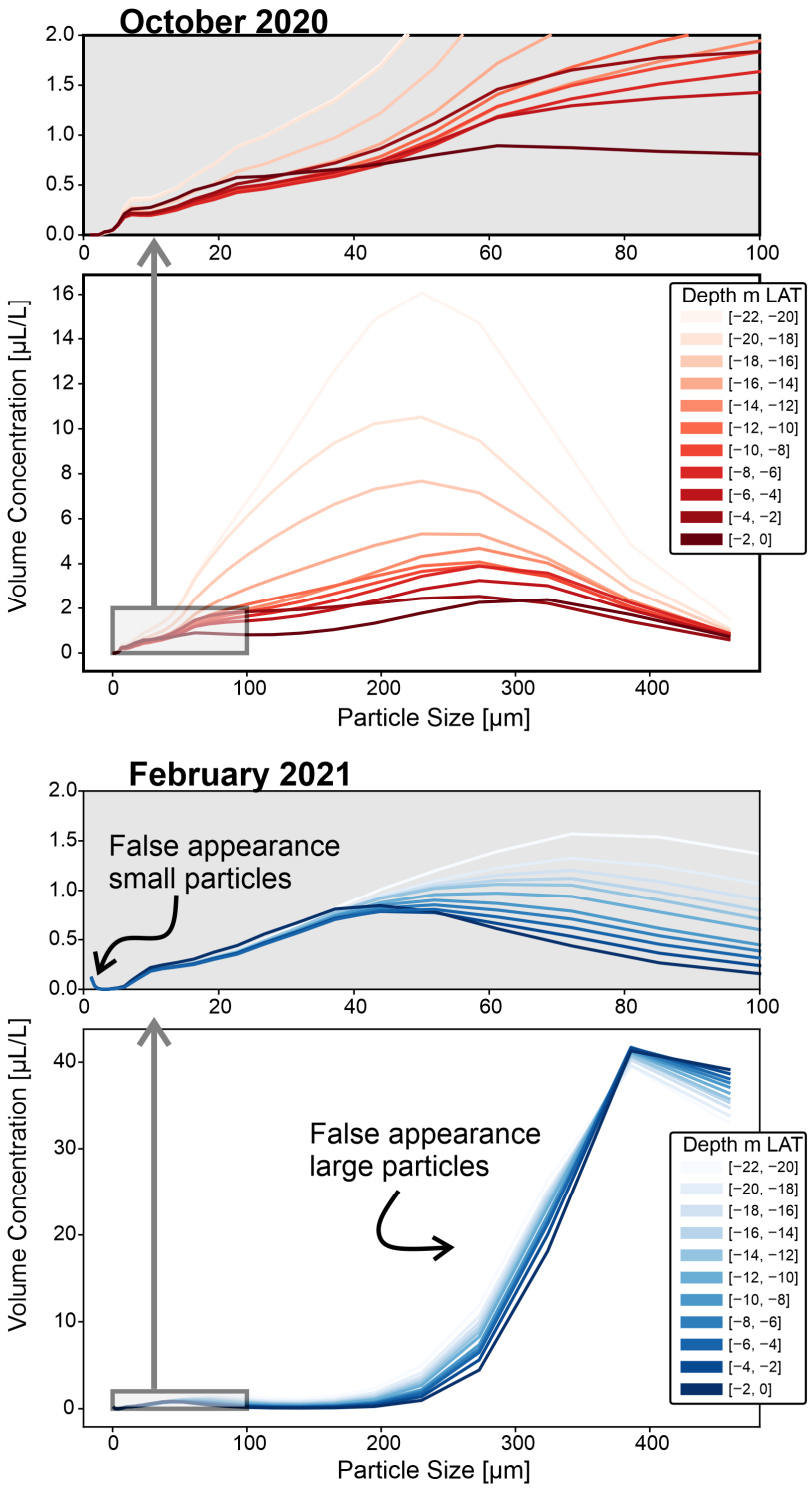


**Figure A1.** Optical misalignment of the LISST 200X laser beam in the February 2021 campaign (**bottom**) enhanced out-of-range effects in the particle size distribution data, which is clear when comparing to the previous campaign in October 2020 (**top**). Particle size distribution plots are shown for two size ranges (0–500 µm and 0–100 µm) and different binned depths (every 2 m; see color bar).

## Appendix C

### *Appendix C.1. Uncertainties Related to the Regression Analyses*

#### Appendix C.1.1. Extraction and Modeling

In natural environments, concentration fluctuations may occur over a wide range of different timescales, from seconds to hours (tidal) and even longer (seasonal). Depending on the desired information, averaging of the data should be performed. As a result of our sampling strategy, we averaged an adequate amount (in the magnitude of $10^5$–$10^6$) of MBES $S_v$ values within a predefined radius around each in-situ sensor measurement in order to compare with the corresponding sensor values. Moreover, the volume of the water column representative for each in-situ sensor measurement is not known. As a result, the optimal radius of the sphere around the measurement to compare to the acoustic $S_v$ values was determined using a cross validation approach. For most TVC models ($TVC_{1–500\ \mu m}$, $TVC_{1–3\ \mu m}$, $TVC_{3–20\ \mu m}$) the largest radius (5 m) was returned as the best radius for the extraction and modeling. This is probably because more MBES $S_v$ values were selected using a radius of 5 m around each in-situ sensor measurement compared to lower radii. This resulted in more averaging, decreasing the impact of outliers and increasing the probability of matching the in-situ measurement.

Artefacts of the in-situ data may result in an erroneous linear regression model. However, given the large amounts of merged datapoints to create the linear regression model (see the high number of observations in Table 2), this error can be considered negligible.

In this study, we used a linear regression model to fit the relationship, assuming no uncertainty in the independent variable ($S_v$). Sources of error can be caused by not taking the uncertainty in the dependent variable into account (only the mean acoustic $S_v$ was retained for each sphere, assuming no standard deviation), or by not meeting the assumptions of linear regression. We would like to note that the modeling in this study was based on big datasets (number of observations between n = 784–12,024). Bigger datasets give us a higher probability of finding a significant statistical relationship between the variables, expressed by the *p*-value of the coefficients. All *p*-values were zero or close to zero, indicating that the relationships are valid.

#### Appendix C.1.2. Gridding and Prediction

We created an acoustic $S_v$ grid with a 2-m bin size before conversion to 3D SPM cubes. The semi-circular geometry of the MBES swaths and the small bin size explain why some grid cells at the edges will be averaged over less data points than in the center. These edge effects were not quantified in the uncertainty.

The predicted Y-value (LogTVC) in the linear regression model exhibits an error range, which depends on the standard error of $\alpha$ and $\beta$ in addition to a random error ($\varepsilon$). This error range was determined using the Statsmodels Python module.

### *Appendix C.2. Uncertainties Related to the Conversion of TVC to SPMC*

The conversion of TVC to SPMC is ideally done by multiplying with an apparent density derived from field calibrations after collection of concurrent stationary water samples and sensor measurements [14,94,108]. However, during the campaigns no concurrent LISST and SPMC data were collected. Hence it was not possible to use the SPMC obtained from filtration and gravimetric measurements to ground-truth and convert the TVC to a surrogate SPMC. Instead, we followed another more mathematical approach based on the fractal floc model [96,97].

In order to estimate the uncertainty on the density calculations, an error envelope (Figure A2) was (artificially) created by varying the primary particle size between $d_p$ = 1–3 µm and the fractal dimension between F = 1.9–2.1. The lower (and upper) limit of the apparent density $\rho_a$ error envelope was calculated using the lowest (and highest) values derived from combining the primary particle $d_p$ and fractal dimension F ranges in the floc apparent density formula. Furthermore, for the three smaller size classes an apparent density of

$\rho_a$ = 2500 kg/m$^3$ [7] was assumed. Then the error bounds for these size classes were fixed to those calculated by the formula for the primary particle size $d_p$ = 2 µm. The error on the apparent density increases exponentially with decreasing particle size.

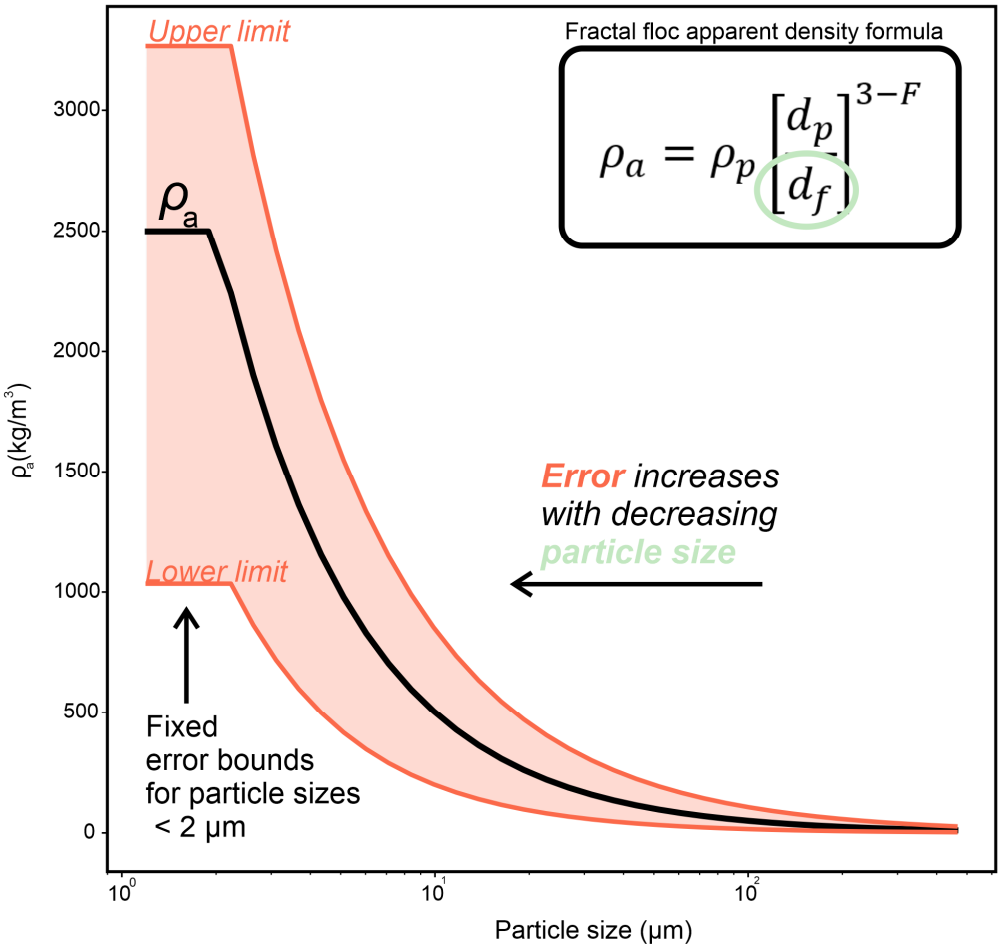


**Figure A2.** Figure showing how the apparent density and error margins exponentially increase with decreasing particle size using the fractal floc model [96,97].

For the estimation of the final SPMC error, the lower (and upper) boundaries of the uncertainty interval of SPMC were determined by multiplying the lower (and upper) uncertainty boundary of density with lower (and upper) uncertainty boundary of TVC, respectively. Hence the magnitude of the error of SPMC is determined by the error on the TVC linear regression model (quantified by Statsmodels as the regression $\varepsilon_i$ error) and the $\rho_a$ error envelope (Figure A2; created by varying primary particle size $d_p$ and fractal dimension F).

The errors of the estimated mass concentration of the total suspended particulate matter ($SPMC_{1–500\ \mu m}$) are large (Table A2). This is mainly because we calculated the mass concentration by multiplying $TVC_{1–500\ \mu m}$ with the average of the densities of all size classes between 1 and 500 µm ($\rho_{1–500\ \mu m}$). However, this calculation assumes that each size class is equally present in the water column, which is very unlikely as the multimodal particle distribution varies (Figure 11). Consequently, the large magnitude of the errors on the apparent densities of primary particles and flocculi (Table 1) are likely the reason for the large errors on the mass concentration ($SPMC_{1–500\ \mu m}$), as the presence of only a few primary particles might substantially increase the density of the suspended mixture.

**Table A2.** Table that shows the average values of the lower limit, upper limit and mean of the confidence interval of the estimated SPMC (in mg/L; for different size ranges) for each campaign.

| SPMC (in mg/L) | | October 2020 20-690 | February 2021 21-092 | March 2021 21-160 | May 2021 21-430 | July 2021 21-550_KW | July 2021 21-550_WD |
|---|---|---|---|---|---|---|---|
| SPMC (1–500 µm) | lower limit | 6.617 | 5.058 | 5.713 | 5.213 | 6.518 | 8.816 |
| SPMC (1–500 µm) | mean | 27.179 | 20.775 | 23.466 | 21.411 | 26.769 | 36.213 |
| SPMC (1–500 µm) | upper limit | 70.398 | 53.812 | 60.781 | 55.457 | 69.337 | 93.811 |
| SPMC (1–3 µm) | lower limit | 0.006 | 0.012 | 0.010 | 0.011 | 0.006 | 0.003 |
| SPMC (1–3 µm) | mean | 0.067 | 0.129 | 0.106 | 0.119 | 0.066 | 0.034 |
| SPMC (1–3 µm) | upper limit | 0.410 | 0.790 | 0.649 | 0.728 | 0.403 | 0.212 |
| SPMC (3–20 µm) | lower limit | 0.804 | 0.490 | 0.629 | 0.516 | 0.766 | 1.340 |
| SPMC (3–20 µm) | mean | 2.823 | 1.718 | 2.205 | 1.810 | 2.689 | 4.702 |
| SPMC (3–20 µm) | upper limit | 6.673 | 4.061 | 5.213 | 4.278 | 6.357 | 11.116 |
| SPMC (20–200 µm) | lower limit | 0.500 | 0.344 | 0.411 | 0.359 | 0.487 | 0.742 |
| SPMC (20–200 µm) | mean | 2.325 | 1.599 | 1.911 | 1.666 | 2.261 | 3.449 |
| SPMC (20–200 µm) | upper limit | 7.281 | 5.008 | 5.986 | 5.217 | 7.083 | 10.803 |
| SPMC (200–500 µm) | lower limit | 0.025 | 0.024 | 0.024 | 0.024 | 0.025 | 0.027 |
| SPMC (200–500 µm) | mean | 0.231 | 0.219 | 0.224 | 0.221 | 0.230 | 0.244 |
| SPMC (200–500 µm) | upper limit | 1.427 | 1.356 | 1.385 | 1.364 | 1.424 | 1.507 |

## References


1. Kirk, J.T.O. Effects of suspensoids (turbidity) on penetration of solar radiation in aquatic ecosystems. *Hydrobiologia* **1985**, *125*, 195–208. [CrossRef]
2. Gray, J.R.; Gartner, J.W. Technological advances in suspended-sediment surrogate monitoring. *Water Resour. Res.* **2009**, *45*, W00D29. [CrossRef]
3. Capuzzo, E.; Lynam, C.P.; Barry, J.; Stephens, D.; Forster, R.M.; Greenwood, N.; McQuatters-Gollop, A.; Silva, T.; van Leeuwen, S.M.; Engelhard, G.H. A decline in primary production in the North Sea over 25 years, associated with reductions in zooplankton abundance and fish stock recruitment. *Glob. Chang. Biol.* **2018**, *24*, e352–e364. [CrossRef] [PubMed]
4. Capuzzo, E.; Stephens, D.; Silva, T.; Barry, J.; Forster, R.M. Decrease in water clarity of the southern and central North Sea during the 20th century. *Glob. Chang. Biol.* **2015**, *21*, 2206–2214. [CrossRef] [PubMed]
5. Lunt, J.; Smee, D.L. Turbidity alters estuarine biodiversity and species composition. *ICES J. Mar. Sci.* **2019**, *77*, 379–387. [CrossRef]
6. Eisma, D.; Kalf, J. Distribution, organic content and particle size of suspended matter in the north sea. *Neth. J. Sea Res.* **1987**, *21*, 265–285. [CrossRef]
7. Fettweis, M. Uncertainty of excess density and settling velocity of mud flocs derived from in situ measurements. *Estuar. Coast. Shelf Sci.* **2008**, *78*, 426–436. [CrossRef]
8. Fettweis, M.; Baeye, M. Seasonal variation in concentration, size, and settling velocity of muddy marine flocs in the benthic boundary layer. *J. Geophys. Res. Ocean.* **2015**, *120*, 5648–5667. [CrossRef]
9. Fettweis, M.; Lee, B.J. Spatial and Seasonal Variation of Biomineral Suspended Particulate Matter Properties in High-Turbid Nearshore and Low-Turbid Offshore Zones. *Water* **2017**, *9*, 694. [CrossRef]
10. Fettweis, M.; Baeye, M.; Van der Zande, D.; Van den Eynde, D.; Joon Lee, B. Seasonality of floc strength in the southern North Sea. *J. Geophys. Res. Ocean.* **2014**, *119*, 1911–1926. [CrossRef]
11. Fettweis, M.; Schartau, M.; Desmit, X.; Lee, B.J.; Terseleer, N.; Zande, D.V.d.; Riethmüller, R. Organic Matter Composition of Biomineral Flocs and its Influence on Suspended Particulate Matter Dynamics along a Nearshore to Offshore Transect. *Earth Space Sci. Open Arch.* **2022**, *127*, e2021JG006332. [CrossRef]
12. Rai, A.K.; Kumar, A. Continuous measurement of suspended sediment concentration: Technological advancement and future outlook. *Measurement* **2015**, *76*, 209–227. [CrossRef]
13. Ouillon, S. Why and How Do We Study Sediment Transport? Focus on Coastal Zones and Ongoing Methods. *Water* **2018**, *10*, 390. [CrossRef]
14. Felix, D.; Albayrak, I.; Boes, R.M. In-situ investigation on real-time suspended sediment measurement techniques: Turbidimetry, acoustic attenuation, laser diffraction (LISST) and vibrating tube densimetry. *Int. J. Sediment Res.* **2018**, *33*, 3–17. [CrossRef]
15. Rymszewicz, A.; O'Sullivan, J.J.; Bruen, M.; Turner, J.N.; Lawler, D.M.; Conroy, E.; Kelly-Quinn, M. Measurement differences between turbidity instruments, and their implications for suspended sediment concentration and load calculations: A sensor inter-comparison study. *J. Environ. Manag.* **2017**, *199*, 99–108. [CrossRef] [PubMed]
16. Osborne, P.D.; Vincent, C.E.; Greenwood, B. Measurement of suspended sand concentrations in the nearshore: Field intercomparison of optical and acoustic backscatter sensors. *Cont. Shelf Res.* **1994**, *14*, 159–174. [CrossRef]

17. Haalboom, S.; de Stigter, H.; Duineveld, G.; van Haren, H.; Reichart, G.-J.; Mienis, F. Suspended particulate matter in a submarine canyon (Whittard Canyon, Bay of Biscay, NE Atlantic Ocean): Assessment of commonly used instruments to record turbidity. *Mar. Geol.* **2021**, *434*, 106439. [CrossRef]
18. Lin, J.; He, Q.; Guo, L.; van Prooijen, B.C.; Wang, Z.B. An integrated optic and acoustic (IOA) approach for measuring suspended sediment concentration in highly turbid environments. *Mar. Geol.* **2020**, *421*, 106062. [CrossRef]
19. Winter, C.; Becker, M.; Ernstsen, V.B.; Hebbeln, D.; Port, A.; Bartholomä, A.; Flemming, B.; Lunau, M. In-situ observation of aggregate dynamics in a tidal channel using acoustics, laser diffraction and optics. *J. Coast. Res.* **2007**, 1173–1177.
20. Gartner, J.W. Estimating suspended solids concentrations from backscatter intensity measured by acoustic Doppler current profiler in San Francisco Bay, California. *Mar. Geol.* **2004**, *211*, 169–187. [CrossRef]
21. Erikson, L.H.; Wright, S.A.; Elias, E.; Hanes, D.M.; Schoellhamer, D.H.; Largier, J. The use of modeling and suspended sediment concentration measurements for quantifying net suspended sediment transport through a large tidally dominated inlet. *Mar. Geol.* **2013**, *345*, 96–112. [CrossRef]
22. Meslard, F.; Bourrin, F.; Many, G.; Kerhervé, P. Suspended particle dynamics and fluxes in an Arctic fjord (Kongsfjorden, Svalbard). *Estuar. Coast. Shelf Sci.* **2018**, *204*, 212–224. [CrossRef]
23. Pawlak, G.; Moline, M.A.; Terrill, E.J.; Colin, P.L. Hydrodynamic influences on acoustical and optical backscatter in a fringing reef environment. *J. Geophys. Res. Ocean.* **2017**, *122*, 322–335. [CrossRef]
24. Baeye, M.; Fettweis, M. In situ observations of suspended particulate matter plumes at an offshore wind farm, southern North Sea. *Geo-Mar. Lett.* **2015**, *35*, 247–255. [CrossRef]
25. O'Connor, T.P. A Wider Look at the Risk of Ocean Disposal of Dredged Material. *Mar. Pollut. Bull.* **1999**, *38*, 760–761. [CrossRef]
26. Lednicka, B.; Kubacka, M.; Freda, W.; Haule, K.; Dembska, G.; Galer-Tatarowicz, K.; Pazikowska-Sapota, G. Water Turbidity and Suspended Particulate Matter Concentration at Dredged Material Dumping Sites in the Southern Baltic. *Sensors* **2022**, *22*, 8049. [CrossRef] [PubMed]
27. Eleveld, M.A.; Pasterkamp, R.; van der Woerd, H.J.; Pietrzak, J.D. Remotely sensed seasonality in the spatial distribution of sea-surface suspended particulate matter in the southern North Sea. *Estuar. Coast. Shelf Sci.* **2008**, *80*, 103–113. [CrossRef]
28. El Serafy, G.Y.; Eleveld, M.A.; Blaas, M.; van Kessel, T.; Aguilar, S.G.; Van der Woerd, H.J. Improving the description of the suspended particulate matter concentrations in the southern North Sea through assimilating remotely sensed data. *Ocean Sci. J.* **2011**, *46*, 179. [CrossRef]
29. Dogliotti, A.I.; Ruddick, K.G.; Nechad, B.; Doxaran, D.; Knaeps, E. A single algorithm to retrieve turbidity from remotely-sensed data in all coastal and estuarine waters. *Remote Sens. Environ.* **2015**, *156*, 157–168. [CrossRef]
30. Baeye, M.; Fettweis, M.; Voulgaris, G.; Van Lancker, V. Sediment mobility in response to tidal and wind-driven flows along the Belgian inner shelf, southern North Sea. *Ocean Dyn.* **2011**, *61*, 611–622. [CrossRef]
31. Fettweis, M.; Nechad, B.; Van den Eynde, D. An estimate of the suspended particulate matter (SPM) transport in the southern North Sea using SeaWiFS images, in situ measurements and numerical model results. *Cont. Shelf Res.* **2007**, *27*, 1568–1583. [CrossRef]
32. Vanlede, J.; Dujardin, A.; Fettweis, M.; Van Hoestenberghe, T.; Martens, C. Mud dynamics in the Port of Zeebrugge. *Ocean Dyn.* **2019**, *69*, 1085–1099. [CrossRef]
33. Van Lancker, V.; Baeye, M. Wave Glider Monitoring of Sediment Transport and Dredge Plumes in a Shallow Marine Sandbank Environment. *PLoS ONE* **2015**, *10*, e0128948. [CrossRef] [PubMed]
34. Thorne, P.D.; Hurther, D. An overview on the use of backscattered sound for measuring suspended particle size and concentration profiles in non-cohesive inorganic sediment transport studies. *Cont. Shelf Res.* **2014**, *73*, 97–118. [CrossRef]
35. Fromant, G.; Floc'h, F.; Lebourges-Dhaussy, A.; Jourdin, F.; Perrot, Y.; Le Dantec, N.; Delacourt, C. In Situ Quantification of the Suspended Load of Estuarine Aggregates from Multifrequency Acoustic Inversions. *J. Atmos. Ocean. Technol.* **2017**, *34*, 1625–1643. [CrossRef]
36. Crawford, A.M.; Hay, A.E. Determining suspended sand size and concentration from multifrequency acoustic backscatter. *J. Acoust. Soc. Am.* **1993**, *94*, 3312–3324. [CrossRef]
37. Holdaway, G.P.; Thorne, P.D.; Flatt, D.; Jones, S.E.; Prandle, D. Comparison between ADCP and transmissometer measurements of suspended sediment concentration. *Cont. Shelf Res.* **1999**, *19*, 421–441. [CrossRef]
38. Moore, S.A.; Le Coz, J.; Hurther, D.; Paquier, A. On the application of horizontal ADCPs to suspended sediment transport surveys in rivers. *Cont. Shelf Res.* **2012**, *46*, 50–63. [CrossRef]
39. Sheng, J.; Hay, A.E. An examination of the spherical scatterer approximation in aqueous suspensions of sand. *J. Acoust. Soc. Am.* **1988**, *83*, 598–610. [CrossRef]
40. Thorne, P.D.; Meral, R. Formulations for the scattering properties of suspended sandy sediments for use in the application of acoustics to sediment transport processes. *Cont. Shelf Res.* **2008**, *28*, 309–317. [CrossRef]
41. MacDonald, I.T.; Vincent, C.E.; Thorne, P.D.; Moate, B.D. Acoustic scattering from a suspension of flocculated sediments. *J. Geophys. Res. Ocean.* **2013**, *118*, 2581–2594. [CrossRef]
42. Thorne, P.D.; MacDonald, I.T.; Vincent, C.E. Modelling acoustic scattering by suspended flocculating sediments. *Cont. Shelf Res.* **2014**, *88*, 81–91. [CrossRef]
43. Ha, H.K.; Maa, J.P.Y.; Park, K.; Kim, Y.H. Estimation of high-resolution sediment concentration profiles in bottom boundary layer using pulse-coherent acoustic Doppler current profilers. *Mar. Geol.* **2011**, *279*, 199–209. [CrossRef]

44. Sassi, M.G.; Hoitink, A.J.F.; Vermeulen, B. Impact of sound attenuation by suspended sediment on ADCP backscatter calibrations. *Water Resour. Res.* **2012**, *48*, W09520. [CrossRef]
45. Sahin, C.; Safak, I.; Hsu, T.-J.; Sheremet, A. Observations of suspended sediment stratification from acoustic backscatter in muddy environments. *Mar. Geol.* **2013**, *336*, 24–32. [CrossRef]
46. Filizola, N.; Guyot, J.L. The use of Doppler technology for suspended sediment discharge determination in the River Amazon/L'utilisation des techniques Doppler pour la détermination du transport solide de l'Amazone. *Hydrol. Sci. J.* **2004**, *49*, 143–153. [CrossRef]
47. Venditti, J.G.; Domarad, N.; Church, M.; Rennie, C.D. The gravel-sand transition: Sediment dynamics in a diffuse extension. *J. Geophys. Res. Earth Surf.* **2015**, *120*, 943–963. [CrossRef]
48. Hage, S.; Cartigny, M.J.B.; Sumner, E.J.; Clare, M.A.; Hughes Clarke, J.E.; Talling, P.J.; Lintern, D.G.; Simmons, S.M.; Silva Jacinto, R.; Vellinga, A.J.; et al. Direct Monitoring Reveals Initiation of Turbidity Currents From Extremely Dilute River Plumes. *Geophys. Res. Lett.* **2019**, *46*, 11310–11320. [CrossRef]
49. Guerrero, M.; Szupiany, R.N.; Amsler, M. Comparison of acoustic backscattering techniques for suspended sediments investigation. *Flow Meas. Instrum.* **2011**, *22*, 392–401. [CrossRef]
50. Simmons, S.M.; Parsons, D.R.; Best, J.L.; Orfeo, O.; Lane, S.N.; Kostaschuk, R.; Hardy, R.J.; West, G.; Malzone, C.; Marcus, J.; et al. Monitoring Suspended Sediment Dynamics Using MBES. *J. Hydraul. Eng.* **2010**, *136*, 45–49. [CrossRef]
51. Best, J.; Simmons, S.; Parsons, D.; Oberg, K.; Czuba, J.; Malzone, C. A new methodology for the quantitative visualization of coherent flow structures in alluvial channels using multibeam echo-sounding (MBES). *Geophys. Res. Lett.* **2010**, *37*, L06405. [CrossRef]
52. O'Neill, F.G.; Simmons, S.M.; Parsons, D.R.; Best, J.L.; Copland, P.J.; Armstrong, F.; Breen, M.; Summerbell, K. Monitoring the generation and evolution of the sediment plume behind towed fishing gears using a multibeam echosounder. *ICES J. Mar. Sci.* **2013**, *70*, 892–903. [CrossRef]
53. Simmons, S.M.; Parsons, D.R.; Best, J.L.; Oberg, K.A.; Czuba, J.A.; Keevil, G.M. An evaluation of the use of a multibeam echo-sounder for observations of suspended sediment. *Appl. Acoust.* **2017**, *126*, 81–90. [CrossRef]
54. Fromant, G.; Le Dantec, N.; Perrot, Y.; Floc'h, F.; Lebourges-Dhaussy, A.; Delacourt, C. Suspended sediment concentration field quantified from a calibrated MultiBeam EchoSounder. *Appl. Acoust.* **2021**, *180*, 108107. [CrossRef]
55. Lurton, X. *An Introduction to Underwater Acoustics: Principles and Applications*; Springer: Berlin/Heidelberg, Germany, 2002; p. 680.
56. Colbo, K.; Ross, T.; Brown, C.; Weber, T. A review of oceanographic applications of water column data from multibeam echosounders. *Estuar. Coast. Shelf Sci.* **2014**, *145*, 41–56. [CrossRef]
57. Innangi, S.; Bonanno, A.; Tonielli, R.; Gerlotto, F.; Innangi, M.; Mazzola, S. High resolution 3-D shapes of fish schools: A new method to use the water column backscatter from hydrographic MultiBeam Echo Sounders. *Appl. Acoust.* **2016**, *111*, 148–160. [CrossRef]
58. Urban, P.; Köser, K.; Greinert, J. Processing of multibeam water column image data for automated bubble/seep detection and repeated mapping. *Limnol. Oceanogr. Methods* **2017**, *15*, 1–21. [CrossRef]
59. Westley, K.; Plets, R.; Quinn, R.; McGonigle, C.; Sacchetti, F.; Dale, M.; McNeary, R.; Clements, A. Optimising protocols for high-definition imaging of historic shipwrecks using multibeam echosounder. *Archaeol. Anthropol. Sci.* **2019**, *11*, 3629–3645. [CrossRef]
60. Lowie, N. Evaluation of the Detection and Quantification of Sediment Plumes Caused by Dredging Activities Using a Multibeam Echosounder. Master's Thesis, Ghent University, Flanders, Belgium, 2017.
61. Roche, M.; Degrendele, K.; Vrignaud, C.; Loyer, S.; Le Bas, T.; Augustin, J.-M.; Lurton, X. Control of the repeatability of high frequency multibeam echosounder backscatter by using natural reference areas. *Mar. Geophys. Res.* **2018**, *39*, 89–104. [CrossRef]
62. Acoustic Reference Area Kwinte (Maritime and Coastal Services-Flemish Hydrography). Available online: https://www.agentschapmdk.be/nl/akoestische-referentiezone-kwinte (accessed on 4 April 2023).
63. Montereale-Gavazzi, G.; Roche, M.; Degrendele, K.; Lurton, X.; Terseleer, N.; Baeye, M.; Francken, F.; Van Lancker, V. Insights into the Short-Term Tidal Variability of Multibeam Backscatter from Field Experiments on Different Seafloor Types. *Geosciences* **2019**, *9*, 34. [CrossRef]
64. Bathymetry Data (Maritime and Coastal Services-Flemish Hydrography). Available online: https://bathy.agentschapmdk.be/spatialfusionviewer/mapViewer/map.action (accessed on 4 April 2023).
65. Mills, B.; Little, A. A High-resolution Aerial System of a New Type. *Aust. J. Phys.* **1953**, *6*, 272–278. [CrossRef]
66. Agrawal, Y.C.; Pottsmith, H.C. Instruments for particle size and settling velocity observations in sediment transport. *Mar. Geol.* **2000**, *168*, 89–114. [CrossRef]
67. SequoiaScientific. LISST-200X Particle Size Analyzer User's Manual Version 2.35. 2022. Available online: https://www.sequoiasci.com/wp-content/uploads/2016/02/LISST-200X_Users_Manual_v2_35.pdf (accessed on 30 October 2021).
68. Praet, N.; Vandorpe, T.; Ollevier, A.; Dierssen, H. TIMBERS in-situ sensor dataset. *Mar. Data Arch.* **2022**. [CrossRef]
69. Fugate, D.C.; Friedrichs, C.T. Determining concentration and fall velocity of estuarine particle populations using ADV, OBS and LISST. *Cont. Shelf Res.* **2002**, *22*, 1867–1886. [CrossRef]
70. Downing, J. Twenty-five years with OBS sensors: The good, the bad, and the ugly. *Cont. Shelf Res.* **2006**, *26*, 2299–2318. [CrossRef]

71. Haalboom, S.; de Stigter, H.C.; Mohn, C.; Vandorpe, T.; Smit, M.; de Jonge, L.; Reichart, G.-J. Monitoring of a sediment plume produced by a deep-sea mining test in shallow water, Málaga Bight, Alboran Sea (southwestern Mediterranean Sea). *Mar. Geol.* **2023**, *456*, 106971. [CrossRef]
72. Hatcher, A.; Hill, P.; Grant, J. Optical backscatter of marine flocs. *J. Sea Res.* **2001**, *46*, 1–12. [CrossRef]
73. Pearson, S.G.; Verney, R.; van Prooijen, B.C.; Tran, D.; Hendriks, E.C.M.; Jacquet, M.; Wang, Z.B. Characterizing the Composition of Sand and Mud Suspensions in Coastal and Estuarine Environments Using Combined Optical and Acoustic Measurements. *J. Geophys. Res. Oceans* **2021**, *126*, e2021JC017354. [CrossRef]
74. Medwin, H.; Clay, C.S. *Fundamentals of Acoustical Oceanography*; Academic Press: San Diego, CA, USA, 1998; p. 712.
75. Salehi, M.; Strom, K. Using velocimeter signal to noise ratio as a surrogate measure of suspended mud concentration. *Cont. Shelf Res.* **2011**, *31*, 1020–1032. [CrossRef]
76. Lohrmann, A.N.A. Monitoring Sediment Concentration with acoustic backscattering instruments. *Nortek Tech. Note* **2001**, *3*, 5.
77. Agrawal, Y.C.; Whitmire, A.; Mikkelsen, O.A.; Pottsmith, H.C. Light scattering by random shaped particles and consequences on measuring suspended sediments by laser diffraction. *J. Geophys. Res. Oceans* **2008**, *113*, C04023. [CrossRef]
78. Andrews, S.; Nover, D.; Schladow, S.G. Using laser diffraction data to obtain accurate particle size distributions: The role of particle composition. *Limnol. Oceanogr. Methods* **2010**, *8*, 507–526. [CrossRef]
79. Andrews, S.W.; Nover, D.M.; Reuter, J.E.; Schladow, S.G. Limitations of laser diffraction for measuring fine particles in oligotrophic systems: Pitfalls and potential solutions. *Water Resour. Res.* **2011**, *47*, W05523. [CrossRef]
80. Felix, D.; Albayrak, I.; Boes, R.M. Laboratory investigation on measuring suspended sediment by portable laser diffractometer (LISST) focusing on particle shape. *Geo-Mar. Lett.* **2013**, *33*, 485–498. [CrossRef]
81. Augustin, J.-M. SonarScope Software. SEANOE. 2022. Available online: https://www.seanoe.org/data/00766/87777/ (accessed on 4 April 2023).
82. Lamarche, G.; Lurton, X. Recommendations for improved and coherent acquisition and processing of backscatter data from seafloor-mapping sonars. *Mar. Geophys. Res.* **2018**, *39*, 5–22. [CrossRef]
83. Foote, K.G.; Chu, D.; Hammar, T.R.; Baldwin, K.C.; Mayer, L.A.; Hufnagle, L.C.; Jech, J.M. Protocols for calibrating multibeam sonar. *J. Acoust. Soc. Am* **2005**, *117*, 2013–2027. [CrossRef] [PubMed]
84. Perrot, Y.; Brehmer, P.; Roudaut, G.; Gerstoft, P.; Josse, E. Efficient multibeam sonar calibration and performance evaluation. *Int. J. Innov. Res. Sci. Eng. Technol.* **2014**, *3*, 808–820.
85. Hughes Clarke, J.E. Applications of Multibeam Water Column Imaging for Hydrographic Survey. *Hydrogr. J.* **2006**, *120*, 3–15.
86. Schimel, A.C.G.; Brown, C.J.; Ierodiaconou, D. Automated Filtering of Multibeam Water-Column Data to Detect Relative Abundance of Giant Kelp (Macrocystis pyrifera). *Remote Sens.* **2020**, *12*, 1371. [CrossRef]
87. Manning, C. Entwine—Point Cloud Organization for Massive Datasets. Available online: https://entwine.io (accessed on 4 April 2023).
88. Schütz, M. Potree: WebGL Point Cloud Viewer for Large Datasets. Available online: http://potree.org (accessed on 4 April 2023).
89. Collart, T.; Praet, N. Data and Python Scripts Used for the TIMBERS Project. 2023. Available online: https://zenodo.org/records/8423005 (accessed on 4 April 2023).
90. Lee, B.J.; Fettweis, M.; Toorman, E.; Molz, F.J. Multimodality of a particle size distribution of cohesive suspended particulate matters in a coastal zone. *J. Geophys. Res. Ocean.* **2012**, *117*. [CrossRef]
91. Fettweis, M.; Baeye, M.; Lee, B.J.; Chen, P.; Yu, J.C.S. Hydro-meteorological influences and multimodal suspended particle size distributions in the Belgian nearshore area (southern North Sea). *Geo-Mar. Lett.* **2012**, *32*, 123–137. [CrossRef]
92. PDALContributors. PDAL Point Data Abstraction Library. Available online: https://pdal.io/en/2.6.0/ (accessed on 4 April 2023).
93. DaskDevelopmentTeam. Dask: Library for Dynamic Task Scheduling. Available online: https://dask.org (accessed on 4 April 2023).
94. Fettweis, M.; Riethmüller, R.; Verney, R.; Becker, M.; Backers, J.; Baeye, M.; Chapalain, M.; Claeys, S.; Claus, J.; Cox, T.; et al. Uncertainties associated with in situ high-frequency long-term observations of suspended particulate matter concentration using optical and acoustic sensors. *Prog. Oceanogr.* **2019**, *178*, 102162. [CrossRef]
95. Fall, K.A.; Friedrichs, C.T.; Massey, G.M.; Bowers, D.G.; Smith, S.J. The Importance of Organic Content to Fractal Floc Properties in Estuarine Surface Waters: Insights From Video, LISST, and Pump Sampling. *J. Geophys. Res. Ocean.* **2021**, *126*, e2020JC016787. [CrossRef]
96. Kranenburg, C. The fractal structure of cohesive sediment aggregates. *Estuar. Coast. Shelf Sci.* **1994**, *39*, 451–460. [CrossRef]
97. Winterwerp, J.C. A simple model for turbulence induced flocculation of cohesive sediment. *J. Hydraul. Res.* **1998**, *36*, 309–326. [CrossRef]
98. Jago, C.F.; Jones, S.E.; Sykes, P.; Rippeth, T. Temporal variation of suspended particulate matter and turbulence in a high energy, tide-stirred, coastal sea: Relative contributions of resuspension and disaggregation. *Cont. Shelf Res.* **2006**, *26*, 2019–2028. [CrossRef]
99. Praet, N.; Collart, T. 3D Volumes of Suspended Particulate Matter in the Belgian Part of the North Sea. 2023. Available online: https://zenodo.org/records/8013207 (accessed on 4 April 2023).
100. Sahin, C.; Ozturk, M.; Aydogan, B. Acoustic doppler velocimeter backscatter for suspended sediment measurements: Effects of sediment size and attenuation. *Appl. Ocean. Res.* **2020**, *94*, 101975. [CrossRef]

101. Rouhnia, M.; Keyvani, A.; Strom, K. Do changes in the size of mud flocs affect the acoustic backscatter values recorded by a Vector ADV? *Cont. Shelf Res.* **2014**, *84*, 84–92. [CrossRef]
102. Vergne, A.; Berni, C.; Le Coz, J.; Tencé, F. Acoustic Backscatter and Attenuation Due to River Fine Sediments: Experimental Evaluation of Models and Inversion Methods. *Water Resour. Res.* **2021**, *57*, e2021WR029589. [CrossRef]
103. Pedocchi, F.; Mosquera, R. Acoustic backscatter and attenuation of a flocculated cohesive sediment suspension. *Cont. Shelf Res.* **2022**, *240*, 104719. [CrossRef]
104. Vincent, C.E.; MacDonald, I.T. A flocculi model for the acoustic scattering from flocs. *Cont. Shelf Res.* **2015**, *104*, 15–24. [CrossRef]
105. Fettweis, M.; Francken, F.; Pison, V.; Van den Eynde, D. Suspended particulate matter dynamics and aggregate sizes in a high turbidity area. *Mar. Geol.* **2006**, *235*, 63–74. [CrossRef]
106. Fettweis, M.P.; Nechad, B. Evaluation of in situ and remote sensing sampling methods for SPM concentrations, Belgian continental shelf (southern North Sea). *Ocean Dyn.* **2011**, *61*, 157–171. [CrossRef]
107. Lanzoni, J.C.; Weber, T.C. Calibration of multibeam echo sounders: A comparison between two methodologies. *Proc. Mtgs. Acoust.* **2012**, *17*. [CrossRef]
108. Mikkelsen, O.; Pejrup, M. The use of a LISST-100 laser particle sizer for in-situ estimates of floc size, density and settling velocity. *Geo-Mar. Lett.* **2001**, *20*, 187–195. [CrossRef]
109. Moate, B.D.; Thorne, P.D. Interpreting acoustic backscatter from suspended sediments of different and mixed mineralogical composition. *Cont. Shelf Res.* **2012**, *46*, 67–82. [CrossRef]
110. Wilson, G.W.; Hay, A.E. Acoustic backscatter inversion for suspended sediment concentration and size: A new approach using statistical inverse theory. *Cont. Shelf Res.* **2015**, *106*, 130–139. [CrossRef]
111. Hawkins, A.D.; Roberts, L.; Cheesman, S. Responses of free-living coastal pelagic fish to impulsive sounds. *J. Acoust. Soc. Am.* **2014**, *135*, 3101–3116. [CrossRef]
112. Francisco, F.; Bender, A.; Sundberg, J. Use of multibeam imaging sonar for observation of marine mammals and fish on a marine renewable energy site. *PLoS ONE* **2022**, *17*, e0275978. [CrossRef]
113. Nilsson, L.A.F.; Thygesen, U.H.; Lundgren, B.; Nielsen, B.F.; Nielsen, J.R.; Beyer, J.E. Vertical migration and dispersion of sprat (*Sprattus sprattus*) and herring (*Clupea harengus*) schools at dusk in the Baltic Sea. *Aquat. Living Resour.* **2003**, *16*, 317–324. [CrossRef]
114. Chen, K.; Zhou, M.; Zhong, Y.; Waniek, J.J.; Shan, C.; Zhang, Z. Effects of Mixing and Stratification on the Vertical Distribution and Size Spectrum of Zooplankton on the Shelf and Slope of the Northern South China Sea. *Front. Mar. Sci.* **2022**, *9*, 870021. [CrossRef]
115. Lezama-Ochoa, A.; Ballón, M.; Woillez, M.; Grados, D.; Irigoien, X.; Bertrand, A. Spatial patterns and scale-dependent relationships between macrozooplankton and fish in the Bay of Biscay: An acoustic study. *Mar. Ecol. Prog. Ser.* **2011**, *439*, 151–168. [CrossRef]
116. Neukermans, G.; Reynolds, R.A.; Stramski, D. Contrasting inherent optical properties and particle characteristics between an under-ice phytoplankton bloom and open water in the Chukchi Sea. *Deep. Sea Res. Part II Top. Stud. Oceanogr.* **2014**, *105*, 59–73. [CrossRef]
117. Clavano, W.; Boss, E.; Karp-Boss, L. Inherent Optical Properties of Non-Spherical Marine-Like Particles—From Theory To Observation. *Oceanogr. Mar. Biol.* **2007**, *45*, 1–38. [CrossRef]